Biophysical *Journal*
Article

Biophysical Society

Amoeboid Swimming Is Propelled by Molecular Paddling in Lymphocytes

Laurene Aoun,[1] Alexander Farutin,[2] Nicolas Garcia-Seyda,[1] Paulin Nègre,[1] Mohd Suhail Rizvi,[2] Sham Tlili,[1,4] Solene Song,[1] Xuan Luo,[1] Martine Biarnes-Pelicot,[1] Rémi Galland,[3] Jean-Baptiste Sibarita,[3] Alphée Michelot,[4] Claire Hivroz,[5] Salima Rafai,[2] Marie-Pierre Valignat,[1] Chaouqi Misbah,[2,*] and Olivier Theodoly[1,*]

[1]Aix Marseille University, CNRS, INSERM, LAI, Turing Centre for Living Systems, Marseille, France; [2]University Grenoble Alpes, CNRS, LIPhy, Grenoble, France; [3]Univ. Bordeaux, CNRS, Interdisciplinary Institute for Neuroscience, IINS, UMR 5297, Bordeaux, France; [4]Aix Marseille University, CNRS, IBDM, Turing Centre for Living Systems, Marseille, France; and [5]Institut Curie, PSL Research University, INSERM U932, Integrative analysis of T cell activation team, Paris, France

ABSTRACT Mammalian cells developed two main migration modes. The slow mesenchymatous mode, like crawling of fibroblasts, relies on maturation of adhesion complexes and actin fiber traction, whereas the fast amoeboid mode, observed exclusively for leukocytes and cancer cells, is characterized by weak adhesion, highly dynamic cell shapes, and ubiquitous motility on two-dimensional and in three-dimensional solid matrix. In both cases, interactions with the substrate by adhesion or friction are widely accepted as a prerequisite for mammalian cell motility, which precludes swimming. We show here experimental and computational evidence that leukocytes do swim, and that efficient propulsion is not fueled by waves of cell deformation but by a rearward and inhomogeneous treadmilling of the cell external membrane. Our model consists of a molecular paddling by transmembrane proteins linked to and advected by the actin cortex, whereas freely diffusing transmembrane proteins hinder swimming. Furthermore, continuous paddling is enabled by a combination of external treadmilling and selective recycling by internal vesicular transport of cortex-bound transmembrane proteins. This mechanism explains observations that swimming is five times slower than the retrograde flow of cortex and also that lymphocytes are motile in nonadherent confined environments. Resultantly, the ubiquitous ability of mammalian amoeboid cells to migrate in two dimensions or three dimensions and with or without adhesion can be explained for lymphocytes by a single machinery of heterogeneous membrane treadmilling.

SIGNIFICANCE Leukocytes have a ubiquitous capacity to migrate on or in solid matrices and with or without adhesion, which is instrumental to fight infections. The precise mechanisms sustaining migration remain, however, arguable. It is for instance widely accepted that leukocytes cannot crawl on two-dimensional substrates without adhesion. In contrast, we showed that human lymphocytes swim on nonadherent two-dimensional substrates and in suspension. Furthermore, our experiments and modeling suggest that propulsion hardly rely on cell body deformations and predominantly on molecular paddling by transmembrane proteins protruding outside the cell. For physics, this study reveals a new type of microswimmer, and for biology, it suggests that leukocyte's ubiquitous crawling may have evolved from an early machinery of swimming shared by various eukaryotic cells.

INTRODUCTION

Individual living cells developed different strategies to migrate and explore their environment. Bacteria, microalgae or mammalian gametes swim in a fluid under the propulsion of a flagellum (1) or of shape deformations (2), whereas somatic mammalian cells crawl with adhesion on a solid tissue via a continuous sequence of forward pushing of the cell front, strengthening of adhesion at the leading edge, and pulling of the cell rear (3,4). In vivo, mammalian cells crawl either on two-dimensional (2D) substrates, like leukocytes on inner blood vessels and epithelial surfaces, or in three-dimensional (3D) environments within tissues. The critical role of adhesion for crawling motility was recently revised in the case of amoeboid mammalian cells, i.e., white blood cells and cancer cells. Amoeboid cells differ from mesenchymatous cells (e.g., fibroblasts) by a significantly higher

Submitted December 17, 2019, and accepted for publication July 15, 2020.

*Correspondence: chaouqi.misbah@univ-grenoble-alpes.fr or olivier.theodoly@inserm.fr

Laurene Aoun, Alexander Farutin, Nicolas Garcia-Seyda, and Paulin Nègre contributed equally to this work.

Editor: Alexander Dunn.

https://doi.org/10.1016/j.bpj.2020.07.033

speed (typically 5–20 vs. 0.1–1 μm min^{-1}) and by highly dynamic shape deformations. Both amoeboid and mesenchymatous cells crawl on adhering substrates, but only amoeboid cells remain motile without adhesion provided that they are confined by a 3D environment (5–8). Although different models exist, this motility in confined nonadherent conditions was generally explained by a chimneying (6) mode in which cell-substrate interactions are mediated by friction instead of adhesion (8–11). It is therefore widely accepted that amoeboid motility of mammalian cells is strictly dependent on adhesion on 2D substrates and on adhesion/friction in 3D media, whereas nonadherent 2D migration and swimming are precluded (5–7,12–19).

In contradiction with this paradigm of adhesive or frictional crawling, Barry and Bretscher (20) reported in 2010 that human neutrophils do swim. They discussed that propulsion may result from membrane treadmilling (rearward movement of the cell surface) or shape deformation (protrusions and contractions along the cell body) but provided no experimental or theoretical evidence supporting either of these hypotheses. Swimming studies on nonmammalian eukaryotic cell, the amoeba *Dictyostelium discoideum*, have later defended a deformation-based propulsion (21), whereas others discarded both treadmilling and shape deformation (22). For tumoral cells, a theoretical model of blebbing mentioned the possibility of migration in suspension by shape changes (23), whereas other modeling efforts validated a swimming mechanism based on shape deformation for the case of amoeba (24–26), cyanobacteria (27), and microalgae (2). A recent study on leukocytes, a mesenchymatous macrophages cell line RAW 264.7, reported that an amoeboid swimming mode could be artificially triggered by optogenetic activation of actomyosin contractility in cell rear (28). In contrast to previous studies, membrane treadmilling seemed mainly involved in propulsion, whereas the contribution of deformations was not assessed. Altogether, swimming of cells without flagellum remains mostly explained by shape deformation mechanisms. Moreover, swimming of mammalian cells without flagellum remains widely discarded (5,6,12,14,17–19,29).

Here, we demonstrate the existence of mammalian amoeboid swimming on primary human T lymphocytes and decipher its functioning experimentally and theoretically at the cellular and molecular scales. T lymphocytes are known to crawl on 2D adhering substrates (16,30–32) and in 3D matrices via adhesion/friction (11,33,34) at typical speeds of 20 μm min^{-1}. We observed swimming motility with an average speed of 5 μm min^{-1} and show that propulsion can be mainly explained by a heterogeneous treadmilling of cell membrane. Actin-bound transmembrane proteins paddle by retrograde transport at the membrane and are recycled from the rear to front of cells by anterograde vesicular transport, whereas nonactin-bound transmembrane proteins are diffusive and hinder swimming. This molecular description is consistent with a speed significantly lower for swimming cells than for crawling cells and cortex retrograde flow. Interestingly, heterogeneous membrane treadmilling supports also ubiquitous cell motility within nonadhesive solid matrices because environmental friction is necessarily larger with a solid than with a fluid.

MATERIALS AND METHODS

Cells

Whole blood from healthy adult donors was obtained from the Établissement Français du Sang (Le Mans, France). Peripheral blood mononuclear cells (PBMCs) were recovered from the interface of a Ficoll gradient/"Milieu de separation des lymphocytes" (Eurobio, Les Ulis, France). T lymphocytes were isolated from PBMCs with Pan T Cell Isolation Kit (Miltenyi Biotec, Bergisch Gladbach, Germany) and then were stimulated for 48 h with anti-CD3/anti-CD28 Dynabeads (Gibco by Thermo Fisher Scientific, Waltham, MA), according to the manufacturer's instructions. T lymphocytes were subsequently cultivated in Roswell Park Memorial Institute Medium 1640 (Gibco by Thermo Fisher Scientific) supplemented with 25 mM GlutaMax (Gibco by Thermo Fisher Scientific), 10% fetal bovine serum (Gibco by Thermo Fisher Scientific) at 37°C, and 5% CO_2 in the presence of IL-2 (50 ng/mL; Miltenyi Biotec) and used 6–10 days after stimulation. At the time of use, the cells were >99% positive for pan T lymphocyte marker CD3 and assessed for activation and proliferation with CD25, CD45RO, CD45RA, and CD69 markers as judged by flow cytometry.

Quantitative cytometry for integrin expression level

For the quantification, we used the CELLQUANT Calibrator kit (ref 7208, Biocytex, Marseille, France). T lymphocytes were stained by indirect immunofluorescence with specific monoclonal antibodies, CD49d (HP2/1) for VLA-4 and CD11a (Hi111) for LFA-1, and then analyzed by quantitative flow cytometry. The expression level of the tested antigen was determined using the kit calibration beads.

Transfection of cells

For single-objective selective plane illumination microscopy (soSPIM) experiments with LifeAct-transduced cells, virus was produced in HEK 293T cells by cotransfecting the lentiviral plasmids pLenti.PGK.LifeAct-Ruby.W (a gift from Rusty Lansford, Addgene plasmid #51009; Watertown, MA) with psPAX2 and pMD2. G (a gift from Didier Trono, Addgene plasmid #12260 and #12259). PBMC were transduced by spinoculation of virus using polybrene, after 48-h activation with CD3-CD28 Dynabeads. The cells were then cultured with IL-2 and used 8 days after activation. The expression of LifeAct-RFP was controlled by flow cytometry. For total internal reflection fluorescence (TIRF)-fluorescence recovery after photobleaching (FRAP) experiments cells, RFP-lentivirus for RFP-actin transduction was bought from Merck (Lentibrite RFP-β-actin lentiviral biosensor; Kenilworth, NJ), and cells were transduced 48 h after activation with a multiplicity of infection of 10. For GFP-actin transfection, plasmid EGFP-Actin-7 from Addgene (ref 56421) was used with the electroporation program Amaxa T20.

Microfluidic channels and surface treatments

Polydimethylsiloxane (PDMS) microchannels were fabricated using standard soft lithography. A positive mold was created with a negative photoresist SU-8 3000 (Microchem Laboratory, Round Rock, TX) on silicon wafers (Sil'tronix, Archamps, France), and then replicas were molded in PDMS elastomer (Sylgard 184, Dow Corning, Midland, MI) and sealed on glass coverslides via plasma activation (Harrick Plasma, Ithaca, NY).

The device is composed of one channel with one inlet and one outlet punched with a 2.4-mm puncher (Harris Uni-Core). For adherent crawling experiments, Ibidi channels $IV^{0.4}$ (CliniSciences, Nanterre, France) were coated overnight at 4°C with 10 μg/mL human ICAM-1-Fc (R&D Systems, Minneapolis, MN) in phosphate buffer solution (PBS) (Gibco). Channels were subsequently blocked with a solution containing 2.5% bovine serum album (BSA) (w/v; Axday, Dardilly, France) and 2.5% Pluronic acid F-108 (w/v; BASF, Ludwigshafen, Germany) in PBS for 30 min at room temperature and then rinsed three times with PBS and finally with Hank's balanced salt solution (HBSS). Cells were injected at densities around 1.5×10^6/mL and allowed to equilibrate for 10 min at 37°C before image acquisition. For nonadherent migration or swimming experiments, Ibidi channels $IV^{0.4}$ and PDMS microchannels were incubated with Pluronic F-127 (Sigma-Aldrich, St. Louis, MO) for 30 min at room temperature and then rinsed three times with PBS and finally with HBSS. Cells were injected at densities around 0.75×10^6/mL in Ibidi channels and 6×10^6/mL in PDMS microchannels of 40 μm height. Cells were allowed to equilibrate for 10 min at 37°C before image acquisition. For migration in nonadherent confined environment, microfluidic tubes and channels of height 2–4 μm were treated with Pluronics F-127 as described above. The adhesive/antiadhesive patterns were prepared by optical patterning. We used an inverted microscope (TI Eclipse, Nikon, Champigny Sur Marne, France) coupled to an ultraviolet laser source and a Digital Micromirror Device (Primo, Alveole, Paris, France) (35). Ultraviolet was projected on ICAM-1 substrates in the presence of a soluble photoactivator (PLPP, Alveole) to degrade the proteins (36). Samples were then rinsed with PBS solution and passivated with BSA and Pluronics F-127 for 15 min at room temperature.

Cell treatments

Stock solutions of blebbistatin (Fisher Bioblock Scientific), CK666 (Sigma-Aldrich), latrunculin (L12370; Molecular Probes, Eugene, OR), primaquine (primaquine biphosphate, Sigma-Aldrich), pitstop2 (Sigma-Aldrich), dynasore (dynasore monohydrate, Sigma-Aldrich), and cytohesin (secinH3, Sigma-Aldrich) were prepared in DMSO following manufacturer's specification, stored at −20°C, and then diluted in culture medium for use in experiments. Cells were resuspended in solutions of 50 μM blebbistatin, 100 μM CK666, 50 nM latrunculin, 100 μM primaquine, or a cocktail of 50 μM pitstop2, 200 μM dynasore, and 20 μM secinH3 and then injected in the microchannels and allowed to settle in the channels for a period of 30 min at 37°C before image acquisition.

Viscosity and osmolarity measurements

Viscosity changes were performed using dextran of average molecular weight of 1500–2800 KDa (Sigma-Aldrich) at concentrations of 50 and 150 g/L. HBSS alone has a viscosity value of 0.001 Pa s, whereas the viscosity for HBSS plus 50 g/L dextran is 0.01, and for HBSS plus 150 g/L dextran, it is 0.1 Pa s. Adding dextran to the media increased the viscosity as well as the osmolarity up to 355 mosm/kg for the solution HBSS plus 150 g/L dextran. Dextrose (Sigma-Aldrich) was then used as an osmolarity control in HBSS media supplemented with 25 mM HEPES. Osmolarity measurements for the different media were performed using the automatic Micro-Osmometer Type 15 (Löser Messtechnik, Berlin, Germany), and calibration was done using standard solutions of 300 and 900 mosm/kg H_2O, according to the manufacturer's instructions.

Experimental fluidic setup

All experiments were performed in a homemade chamber precisely thermostated at 37° to limit temperature instability, potentially inducing flow drifts within fluidic devices. For swimming close to a surface, we used Ibidi channels for experiments in HBSS, dextrose, and 50 g/L dextran solutions and 40 μm high PDMS microchannels for experiments in 150 g/L dextran to limit the observation range in the z axis because cells did not sediment. To minimize flow, channels were sealed with a plastic cap for Ibidi channels or with a 250 μm thickness PDMS film for the PDMS microchannels. On the microscope stage, the devices were surrounded by a 100% humidity chamber to minimize evaporation through PDMS. For experiments of swimming in suspension, cells were resuspended in 66% Ficoll to limit sedimentation effects and injected in 100 μm high channels. Minimization of drifts for swimming in suspension was more challenging than for the swimming close to a substrate. The microfluidic channel was set vertical (along the gravity axis), and the whole microscope was tilted by 90° to get a side-observation view. The channel was connected to a microfluidic flow control system (Fluigent MFCS-EZ) to control the unidirectional flow toward the bottom, and we used 2-m long tubes of 0.5 μm internal diameter to further limit drift by hydraulic resistance. Cell motion was recorded for at least 100 frames every 10 s.

Cell motion imaging

Experiments were performed with an inverted Zeiss Z1 automated microscope (Carl Zeiss, Oberkochen, Germany) equipped with a CoolSnap HQ CCD camera (Teledyne Photometrics, Tucson, AZ) and piloted by μManager [1.4]. Different objectives were used for bright-field mode (Plan Apochromat 20×/0.8, 63×/1.4 objectives) and for reflection interference contrast microscopy (RICM) mode (Neofluar 63/1.25 antiflex). A narrow band-pass filter ($\lambda = 546$ nm $\pm$ 12 nm) was used for RICM. 3D imaging was performed on cells stained with a lipophilic tracer DiO (Invitrogen, Carlsbad, CA), and cells were transfected with LifeAct-RFP cells. The imaging was done using a spinning disk (Inverted Nikon Eclilpse TI) equipped with two cameras (Photometrics EMCCD evolve) and controlled by MetaMorph and a home-made soSPIM setup.

soSPIM imaging and analysis

The soSPIM system, for single-objective selective plane illumination microscope, is a recently developed architecture that enables combining the advantages of low phototoxicity and high optical sectioning of light-sheet microscopy techniques with the high sensitivity provided by high numerical aperture objectives (37). The setup is composed of a high numerical aperture objective (CFI Plan Apochromat VC 60× WI 1.27 NA), a beam steering unit, and dedicated microfabricated devices containing mirrors angled at 45° alongside microwells. The soSPIM components are mounted on a conventional inverted microscope (Nikon Ti-E). The microfabricated chambers (see (37) for detailed descriptions of the chambers) are placed on an axial translation piezo stage (Mad City Labs, Madison, WI) within a controlled environment chamber (Tokai Hit, Shizuoka, Japan) for live cell imaging. Fluorescence emission is collected through the same objective used for excitation and is captured on a sCMOS camera (ORCA-Flash 4.0 V2, Hamamatsu, Japan). The whole acquisition process is steered under MetaMorph environment (Molecular Devices, San Jose, CA) using a homemade designed plugin that synchronizes the excitation and acquisition processes. Further details of soSPIM setup, calibration, and synchronization are described in (37). The 3D time series data sets acquired with the soSPIM setup were analyzed using the freely available software UCSF Chimera (38) (developed by the Resource for Biocomputing, Visualization, and Informatics at the University of California, San Francisco (supported by NIGMS P41-GM103311)). This software enables us to render surfaces of equal fluorescence intensity as well as normalization and alignment of whole 3D time series, which enhances the possibility to visualize cell membrane movement in our case.

Molecular motility imaging

For TIRF-FRAP experiments, cells were resuspended in HBSS-dextran 150 g/L solution at a concentration of 4.5×10^6 cells/mL in the presence of CD11a/CD18 (BioLegend, clone M24) and HLA-A,B,C (BioLegend, clone

W6/32) primarily conjugated antibodies. Alternatively, cells were labeled with Vybrant DiO by 10-min incubation at 37°C in the presence of 5 μL of dye per 1.5×10^6 cells and then washed twice with HBSS and resuspended in HBSS-dextran. For LifeAct-RFP cells, no further staining was required. Cell suspensions were loaded into the devices and centrifuged for 3 min at 200 RCF. Cells were allowed to equilibrate for at least 10 min at 37°C before image acquisition. Videos were recorded on a Nikon Eclipse Ti microscope, equipped with iLas2 system and controlled by MetaMorph software. For DiO and MHC-1 staining, diffusion coefficients were calculated using the SimFRAP ImageJ plugin. LFA-1 cluster speed values were calculated from kymographs performed along the cell axis, whereas actin flow was calculated measuring the displacement of the frapped region. All values were corrected by the advance of the front edge, measured by a kymograph along the cell axis, to obtain a value relative to the cell front.

Cell tracking

For swimming experiments in the vicinity of a substrate (in 2D), cells were tracked with a homemade program (MATLAB software; The MathWorks, Natick, MA), and raw curvilinear speeds of swimming cells were calculated using trajectory time points every 30 s. Residual flow drift was corrected on each cell trajectory using the mean x- and y-movement values of all cells between two pictures. For high viscosity experiments, the fraction of cells squeezed toward the substrate by depletion force were discarded from the analysis. For swimming experiments in suspension (in 3D), a stack of bright-field images was taken every 10 s across the 100-μm height of the channel with a spatial pitch of 5 μm. To determine the position of a particular cell on the x axis at a given time, we analyzed the intensity distribution of the image of this cell on all images of the x axis stacks. The best focus corresponded to the image with the minimal SD of the intensity, which yielded an x position with a precision of 2.5 μm. Each cell trajectory was fragmented in 30-s steps, and cell-step speed was calculated using coordinates along the x and y axes. The speed component along y was considered negligible because we selected cells with an orientation perpendicular to the y axis. Total cell speed was calculated as the mean of all the 30-s step's speed for each cell.

The circularity of cells was determined on bright-field images at magnification ×63. Images were first binarized using the Pixel classification workflow of the Ilastik software (39). The binaries images were then analyzed in MATLAB, and the circularity was calculated using the image processing toolbox, $Circularity = Perimeter^2/(4\pi Area)$.

Beads advection experiments

Streptavidin-coupled beads with a diameter of 2.7 μm (Dynabeads M-270 Streptavidin; Invitrogen) were washed three times with 0.1% BSA (w/v) and then incubated with 0.5 μg/mL biotin-coupled Protein-A (Sigma-Aldrich) for 1 h under stirring at room temperature and rinsed with 0.1% BSA. The beads were then incubated with 500 μg/mL ICAM for 2 h at room temperature and rinsed with 0.1% BSA. A final concentration of 0.125 mg/ml Dynabeads was added to the cell suspension. Bright-field images (Plan Apochromat ×20/0.8) were taken every 3 s. Beads were tracked manually from the moment the bead attached to the cell front until it reached the cell rear. Cells are moving in the frame of the laboratory, and cell rear was taken as a reference of bead position. All experiments were performed at least in triplicate for each substrate and/or drug.

RESULTS

Leukocytes are motile on a solid substrate without adhesion or friction

Upon recruitment from the blood stream toward inflammation zones, leukocytes arrest and crawl on the inner surface of blood vessels. This 2D migration, called crawling, was here mimicked in vitro with human primary effector T lymphocytes on glass substrates coated with ICAM-1 molecules, a specific ligand for the integrin adhesion molecules LFA-1. Effector T lymphocytes developed a stable polarization in suspension, with a front pole forming protrusions (lamellipods) under the influence of actin polymerization and a rear pole (uropod) undergoing contraction cycles enforced by actomyosin contractility. When introduced into a chamber coated with ICAM-1, lymphocytes sedimented, adhered to, and migrated on the substrates. They crawled with a random walk pattern (Fig. 1 *A*; Video S1) of curvilinear speed 14.7 ± SD 7.5 μm min^{-1}, with a widespread lamellipod in front, the nucleus positioned in the cell central zone, and a narrow uropod in rear. To challenge the idea that adhesion is necessary for amoeboid migration on a 2D substrate, we then replaced the ICAM-1 surface treatment by an antiadhesive coating of Pluronic F127 (Fig. 1 *B*). Without adhesion, cells were highly sensitive to residual flows, which must be dampened to allow observation and characterization of self-propulsion. After sedimentation, cells displayed a random walk with an apparent average curvilinear speed of 5.5 ± SD 2.2 μm min^{-1} (Fig. 1 *Bi*; Video S1). To assess the adhesion state of cells versus surface treatment, we performed contrast interferometric imaging, RICM (Fig. 1, *A* and *Biii*; Video S1). A dark contact zone of cells on ICAM-1 substrates corresponded to a cell-substrate distance around 50 nm, which is characteristic of tightly adhered cells with extracellular proteins and polysaccharides confined between the substrate and the adherent plasma membrane (40,41). In contrast, a bright contact zone of cells on Pluronics in RICM corresponded to a distance around 100 nm, which is typical of the presence of a thin liquid film separating the substrate from the fluctuating plasma membrane of a cell settling by gravity. According to the RICM assays, 100% of polarized and motile cells were nonadherent on Pluronics (Fig. S1). Nonadherent cells migrating in the vicinity of a nonadherent substrate were further imaged in 3D by spinning disk microscopy (Video S2). Although strong phototoxicity hampered long-term 3D imaging, migration of polarized cells with dynamic 3D shape deformations could be monitored on tens of micrometers. Altogether, these data show that polarized lymphocytes do migrate on a 2D surface in the absence of adhesion.

Cells can switch between adherent and nonadherent migration

To shed light on the transition between adherent and nonadherent migration, we then presented lymphocytes to substrates patterned with alternated stripes of adhesive and antiadhesive coatings (Fig. 1 *C*; Video S3). Although mesenchymatous cells are known to be strictly confined to adherent stripes in similar experiments (42), lymphocytes showed here a unique capability to transfer repeatedly between adherent and nonadherent zones. The stripes width

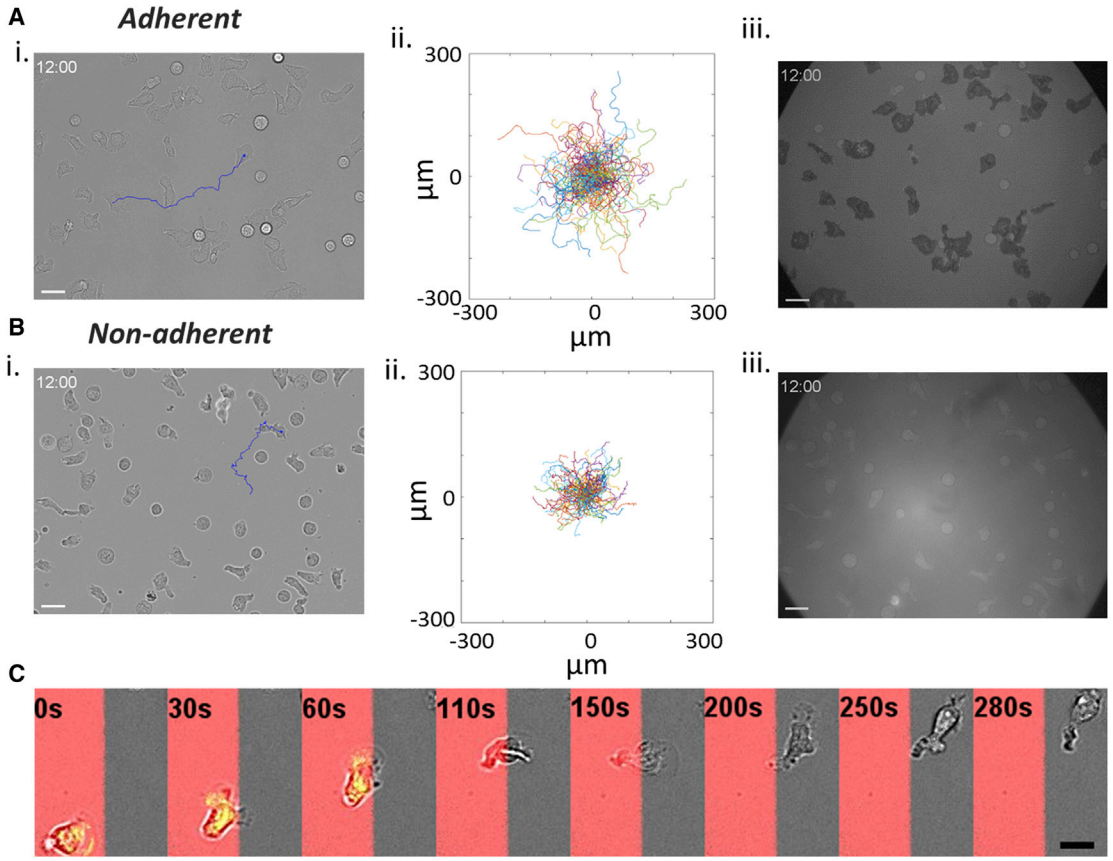

FIGURE 1 From adherent to nonadherent 2D migration. Primary human effector T lymphocytes are shown. (*A*) Adhesive crawling on ICAM-1-treated substrate and (*B*) nonadherent migration on Pluronic F127-treated substrate. (*i*) Bright-field images. Blue lines correspond to the track of a particular cell for 12 min. Scale bars, 20 μm. See also Video S1. (*ii*) Representative tracks of motile cells in a single experiment (time lag = 20 s, duration 16 min, $n > 100$ cells). (*iii*) RICM images. Cell contact zone is dark for cells crawling on ICAM-treated surfaces, revealing an adhesion phenotype, and white for cells on nonadhesive surfaces, attesting the absence of adhesion to the surface (see also Fig. S1). Bars are standard deviations. ****p < 0.0001 (two-tailed Student's t-test). Scale bars, 20 μm. (*C*) Image sequence of a cell migrating over adjacent stripes of adhesive ICAM-1 (*red*) and antiadhesive polyetheleneglycol (*gray*) prepared by LIMAP (72) with a width of 40 μm. The sequence is a merge of fluorescent images (ICAM-1, *red*), bright-field images (cell morphology, *gray*), and RICM images (adhesion zone, *green*). Scale bars, 20 μm. See also Video S3. To see this figure in color, go online.

of 40 μm was chosen to be large enough to allow cells to travel on homogeneous stripes for tens of seconds and small enough to favor the occurrence of transitions between different stripes. Interference microscopy attested that cells traveled across the adhesive zones with adhesive contact to the substrate (green signal) and across antiadhesive zones with a lubrication film separating the cells from the substrate (no green signal). Cells were even found to have the same probability of presence on adherent and antiadherent stripe (43). These observations suggest that the transition between adherent and nonadherent motility modes is fast or that the two phenotypes share the same machinery, which altogether cancels the idea of switch between two modes.

Diffusive versus active motion in nonadherent migration

The average speed of cells measured using the average displacements of cell mass center every 30 s was significantly different between adherent and nonadherent cells (Fig. 2 *A*). However, this estimation of the active motion of cells was biased by several effects for nonadherent cells. First, our system of effector lymphocytes in suspension comprised two populations, one of round and inactive cells with a typical circularity >0.8 and the other of polarized and active cells with a typical circularity <0.8. The average fraction of active cells in suspension is around 48 $\pm$ SEM 5%. Fig. 2 *B* presents the histogram of raw speeds for individual cells in the case of live and fixed lymphocytes (all cell shapes are frozen by paraformaldehyde in the latter case). Although fixed cells were not motile, they displayed an apparent raw curvilinear speed of 2.8 $\pm$ 0.3 μm min^{-1} because of Brownian diffusion. Live cells displayed two populations, one with low speed corresponding to round and inactive cells and one with higher speed corresponding to polarized and active cells. The apparent speed of inactive cells was close to the one of fixed cells, meaning that their movement was close to Brownian motion. In contrast, active cells had a

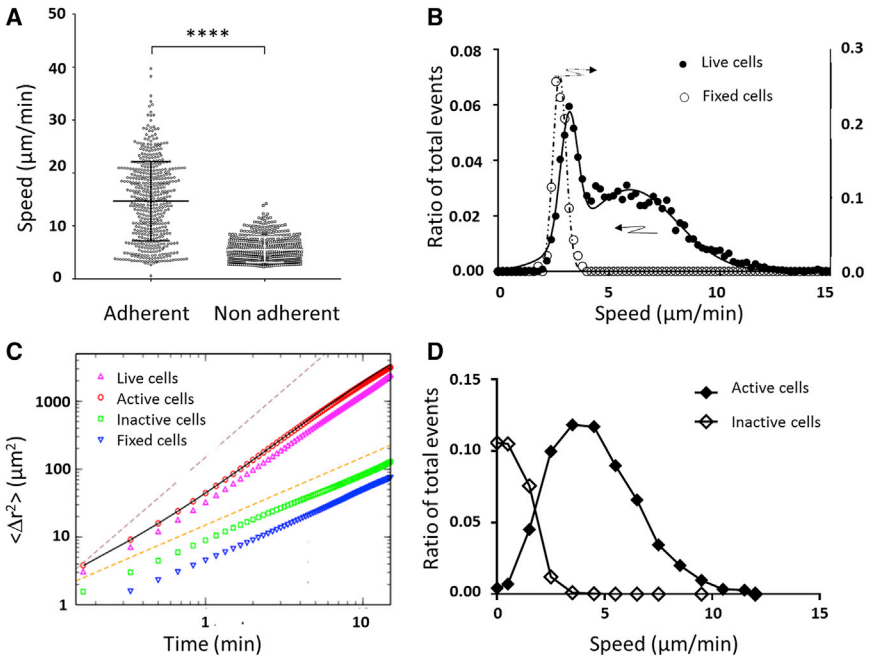

FIGURE 2 Active polarized cells migrate without adhesion in 2D at 5 μm min^{-1}. (*A*) Raw curvilinear speed of cells crawling on adherent ICAM-1-treated substrates and migrating on anti-adherent Pluronic F127-treated substrates, estimated by averaging the displacements of cell mass centers over intervals of 30 s. Bars are standard deviations. $N = 500$ cells, ****p < 0.0001 (two-tailed Student's t-test). (*B*) Histogram of raw curvilinear speed of live nonadherent migrating cells (*filled dots*, *left y axis*) and fixed cells (*hollow dots*, *right y axis*). Data are fitted with a single Gaussian for fixed cells (*dotted line*) and a double Gaussian for live cells (*dark line*). Live cells are composed of one population of diffusing cells and one of migrating cells with an average speed of 5.9 μm min^{-1}. (*C*) Mean-square displacement $<[r(t) - r(0)]^2>$ as a function of time for all cells and all steps was combined in the case of live cells (*upward pointed triangles*) and fixed cells (*downward pointed triangles*). Fixed cells have purely diffusive behavior corresponding to $D_t = 2.34$ μm^2 min^{-1}. Circles and squares show the mean-square displacement for active and inactive cells, respectively. Black line is a fit of active cells using Eq. 9 (Supporting Materials and Methods) with $v_s = 4.3$ μm min^{-1}, $D_r = 0.19$ min^{-1}, and $D_t = 7.28$ μm^2 min^{-1}. Dashed lines show the limit cases of purely ballistic and diffusive behavior with slopes of, respectively, 2 and 1. (*D*) Histogram of average speed per cell determined using Eq. 1 as in (*C*) for active cells (*filled diamonds*) and inactive cells (*hollow diamonds*). Root mean-square speed of active cells is equal to 4.9 μm min^{-1}. Lines are guides for the eye. To see this figure in color, go online.

significantly larger average raw curvilinear speed of 5.9 $\pm$ 4.2 μm min^{-1}. However, this new estimated speed does not strictly characterize active motility because it still comprises diffusion effects as evidenced by fixed cells or round inactive cells. We therefore performed a more detailed analysis of cell trajectories to discriminate the diffusive contribution from the effective active motion. First, we investigated the mean-square displacement averaged over all cells in the population as a function of time. Second, we fitted the mean-square displacements as a function of time interval by a random walk law, which combines 2D Brownian-like diffusion with persistent motion, and we analyzed the distribution of speeds v_s and diffusion coefficients D_t obtained by the fitting procedure:

$$[r(t) - r(0)]^2 = v_s^2 t^2 + 4D_t t, \qquad (1)$$

We then separated all cells in the population into two groups. We considered as active the cells that traveled at least a distance of 25 μm (about two cell diameters) during the acquisition time of 13 min and the rest of the cells being referred to as inactive. Fig. 2 *C* shows the mean-square displacement as a function of time for fixed and live cells, and we also report inactive and active cells separately for live cells. Both inactive and fixed cells had a diffusive behavior, with an average diffusion coefficient of, respectively, 2.3 and 1.1 μm^2 min^{-1}, whereas active cells had a superdiffusive behavior. A satisfactory fit could not be obtained with Eq. 1, and we extended the model by adding rotational diffusion (with a rotational diffusion coefficient D_r), which accounted for gradual changes in the direction of the cells (see Supporting Materials and Methods). The fitting procedure gave here $v_s = 4.3$ μm min^{-1}, $D_r = 0.19$ min^{-1}, and $D_t = 7.28$ μm^2 min^{-1} (*black curve* in Fig. 2 *C*). To obtain the distribution of speeds of active cells, we then simplified the analysis and considered only displacements for time intervals of 2 min, which is 3 times smaller than $1/D_r$ and therefore allowed us to neglect rotational diffusion. As can be observed in Fig. 2 *D*, most of the active cells had a speed around 3 to 5 μm min^{-1}, and root mean-square speed extracted of individual active cells was finally 4.9 μm min^{-1} in cell culture medium. This precise determination of cell speed without adhesion will later be instrumental to propose a consistent mechanism.

Active lymphocytes swim in free suspension

Although active lymphocytes migrated in the vicinity of a surface without adhesion, one may argue that propulsion close to a substrate may be favored by hydrodynamic coupling between cells and substrate. We therefore performed experiments with cells in bulk suspension to test the existence of swimming without hydrodynamic coupling to any solid wall. It appeared quite challenging to cancel artifactual cell displacements in suspension. Conditions of negligible flow were difficult to achieve because of several

perturbative effects such as temperature gradients, pressure imbalance between channel outlets, or gravimetric imbalance resulting from cell dispersion inhomogeneity. In the end, we used a microfluidic channel connected to a high-precision pressure controller and highly resistant tubing connections to slow down pressure-driven flows. Besides, cell sedimentation was decreased using Ficoll-supplemented medium to match the average density of cells. Still, cells had dispersed densities, and they exchanged material with the medium, so that sedimentation drifts were changing with each cell and with time. As a consequence, flow and sedimentation drifts could not be totally cancelled, and we decided to merge their combined artifactual effects on a single axis by tilting the microscope by 90° and setting the main axis of the microfluidic channel along the vertical axis (Fig. 3 *A* and Supporting Materials and Methods for details). In this configuration, the vertical *z* axis cumulated artifacts because of pressure-driven flow across the microchannel main direction, which was low but non-null, and because of the gravity-induced sedimentation, which was different from one cell to another. Swimming prowess was then measured on the *y* and *x* axes (Fig. 3 *B*; Video S4). Cell position on the *y* axis was determined from the selection of the best-focused images on *y* stack scans for each time point. In line with the results on a nonadherent substrate, round cells (circularity >0.8) were used as a negative control for inactive and nonswimming cells, whereas polarized cells (circularity <0.8) were tested as the active and potentially swimming cells. Fig. 3 *C* shows that inactive cells displayed a curvilinear speed of 2.1 ± SD 0.6 μm min^{-1}, which is close to the value found for diffusive cells in 2D. In contrast, active polarized cells displayed an apparent average curvilinear speed of 8.9 ± SD 2.4 μm min^{-1}. These data confirm the intrinsic capability of polarized lymphocytes to swim in suspension at several μm min^{-1}. Furthermore, experiments showed that the vicinity of a wall within a few micrometers range had no significant effect on swimming speed (Fig. S2). We performed theoretical calculations to get quantitative insight on the influence of substrate on swimming speed down to a distance of 100-nm range, which corresponds to the case of sedimented cells migrating over nonadherent substrates in Figs. 1 and 2. Our calculations support that the vicinity of a single wall has a negligible effect on swimming speed (see Supporting Materials and Methods, Vicinity of a wall is negligible). In what follows, systematic measurements to characterize swimming properties were therefore performed with the more convenient setup of cells close to a nonadherent substrate.

Swimming propulsion is oriented along polarization axis toward lamellipod edge

Swimming appears to be a specific property of polarized and active cells, whereas inactive and round cells are just passively diffusing. We further analyzed the angular difference between the direction of polarization of active cells and their instant displacement direction (Video S5). Active cells showed a maximal probability for swimming direction colinear to cell polarization, whereas fixed cells displayed no preferential orientation of motion (see Fig. S3). This analysis supports further that the process of swimming is specific to active and polarized cells and that swimming propulsion is oriented along the cell's polarization axis in the direction of lamellipod.

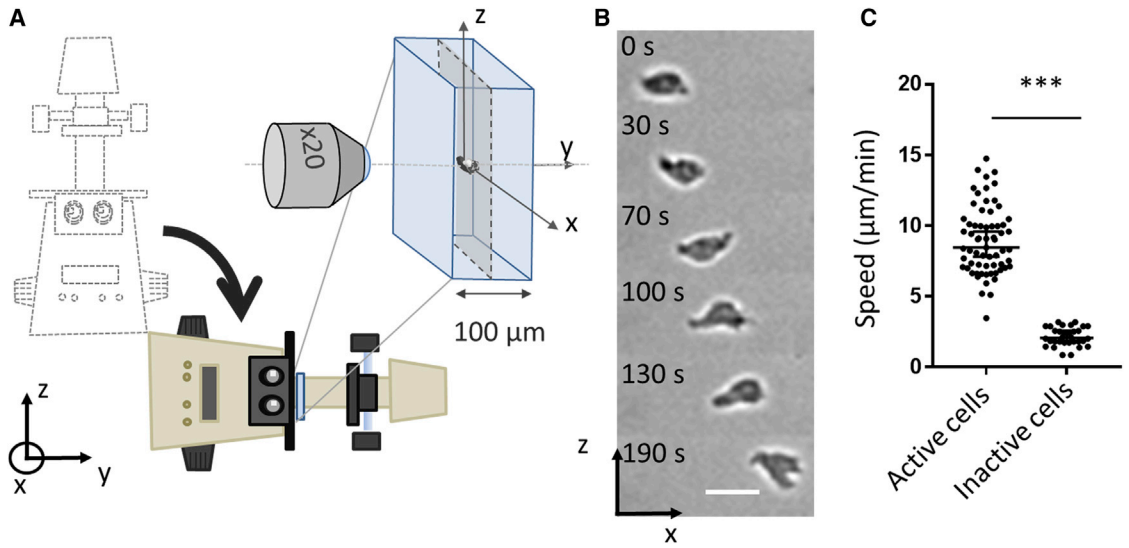

FIGURE 3 Lymphocytes swim in free suspension. (*A*) Schematic of the setup used to image swimming in suspension with a microscope tilted by 90° and a flow channel oriented vertically. (*B*) Sequence of images of a cell swimming in the center of the channel in the direction of the *x* axis. Scale bars, 20 μm. See also Video S4. (*C*) Speed of active and inactive cells for a distance to the wall larger than 40 μm. Experiments $N = 6$, cells $N > 16$, and steps $N > 80$. ***$p <$ 0.001 (two-tailed Student's *t*-test). To see this figure in color, go online.

Viscosity hardly affects swimming speed

Swimming relies necessarily on the coupling between a cell motility machinery and the surrounding fluid. One may therefore expect the viscosity of the fluid to have an effect on the coupling efficiency. Swimming speed was measured versus the different viscosities of the external medium by the addition of dextran of the molecular weight 2000 kDa. Viscosity was increased by 100-fold as compared to normal medium. Higher dextran concentrations were inaccessible because cells were strongly pressed to the substrate by depletion force and consequently immobilized. For a 10-fold viscosity increase, there was a slight decrease of speed by 25%; however, this tendency was not confirmed for a 100-fold viscosity increase, for which speed was similar to control. Hence, counterintuitively, cell swimming speed was hardly affected by a change of viscosity of two orders of magnitude (Fig. S4; Table S1). The insensitivity of cell speed to external viscosity is traced back to the fact that dissipation because of swimming occurs predominately in the cell cortex, which has a much higher viscosity compared to the suspending medium. This means that we expect an effect of external viscosity only when it becomes comparable to that of the cortex.

Actin mediates swimming propulsion by polymerization and, to a lesser extent, contractility

Actin cytoskeleton is widely accepted as the molecular engine propelling cell crawling. Effector T lymphocytes are characterized by a strongly polarized state with actomyosin contractility, mainly in the cell rear (uropod), and actin polymerization, mainly in the cell front (lamellipod). We first perturbed cells with blebbistatin, a potent inhibitor of actomyosin contractility. The uropod was not distinguishable anymore, and the cell body looked devoid of contractile activity, but motile cells displayed a small lamellipod, which attested a conserved front-rear polarization. (Fig. 4, *A* and *B*; Video S6). The dampening of cell's deformations because of contractility inhibition induced a significant increase of the circularity index (Fig. 4 *B*, *right*), whereas swimming speed decreased by 25% as compared to control cells (Fig. 4 *C*; Table S1). Swimming direction and cell polarization were still markedly correlated, even more than for control cells (Fig. S3). These results suggest that actin contractility and contractile cell deformations are not required for swimming and, conversely, that frontal actin polymerization plays a dominant role. We then perturbed actin polymerization in the cell front with latrunculin (Fig. 4 *A*; Video S6). The dose was chosen low enough to inhibit the lamellipod formation at the cell front while preserving contractility in the cell rear. Latrunculin-treated cells were therefore deprived of lamellipod but conserved a uropod, which is the opposite situation to blebbistatin-treated cells. The fraction of swimming cells was significantly lower than for both control and blebbistatin-treated cells (Fig. 4 *C*; Table S1), which suggests that actin polymerization plays a more preponderant role than contractility in propulsion. We then treated cells with CK666, an inhibitor of the protein Arp2/3 that mediates branching of the actin network in lamellipods (Fig. 4 *A*; Video S6). Although the front of migrating leukocytes usually displayed lamellar-shaped protrusions (44), CK666-treated cells formed filopodia and blebs in cell front. The average effect of CK666 on swimming speed was found intermediate between the blebbistatin and latrunculin cases in terms of the fraction of migrating cells. Altogether, swimming was more efficient with a perturbed lamellipod (CK666) than without lamellipod (latrunculin). This correlation between a stronger perturbation of the lamellipod and slower swimming is in line with the lamellipod being important for propulsion. Besides, swimming was more efficient for totally inhibited uropod (blebbistatin) than for partially inhibited lamellipod (CK666), which corroborates the idea that swimming would be mediated to a larger extent by lamellipod rather than by uropod. Finally, swimming was fully abrogated with a combination of blebbistatin and latrunculin (Fig. 4, *A* and *C*; Video S6), which suggests that the actin network is the main engine of lymphocyte swimming.

Rearward traveling of membrane protrusions alone seems not efficient enough to propel lymphocyte swimming

Swimming propulsion arises from the interactions of the cell external membrane with the surrounding fluid; therefore, the dynamic properties of the cell external membrane is the key of the swimming mechanism. Like all amoeboid cells, lymphocytes display highly dynamic shape deformations, which are good candidates for generating propulsion. To precisely monitor cell deformations and circumvent the strong photosensitivity issues, we resorted to light-sheet soSPIM microscopy on cells transfected with RFP-Lifeact. The 3D dynamics of cell cytoskeleton (Fig. 5 *A*, *left*; Video S7) revealed waves of lamellar protrusions that formed with different orientations in the cell front (44,45) and traveled backward until they vanished in the cell rear. Similar propagating waves of cell membrane were also visible in transmission microscopy (Fig. 5 *A*, *right*; Video S8) (18,46,47) together with constriction rings, provoking sudden nucleus movement and important reorganizations of cell's contours toward the direction of cell motility (see also Video S8). This dynamics of cell contours is qualitatively reminiscent of the shape deformation cycles analyzed in theoretical modeling of amoeboid swimming (2). To get more quantitative insight, we developed a direct numerical simulation of normal active forces applied to the cell membrane (with force-free and torque-free conditions) that generated deformations traveling backward along the cell body (Figs. 5 *B*

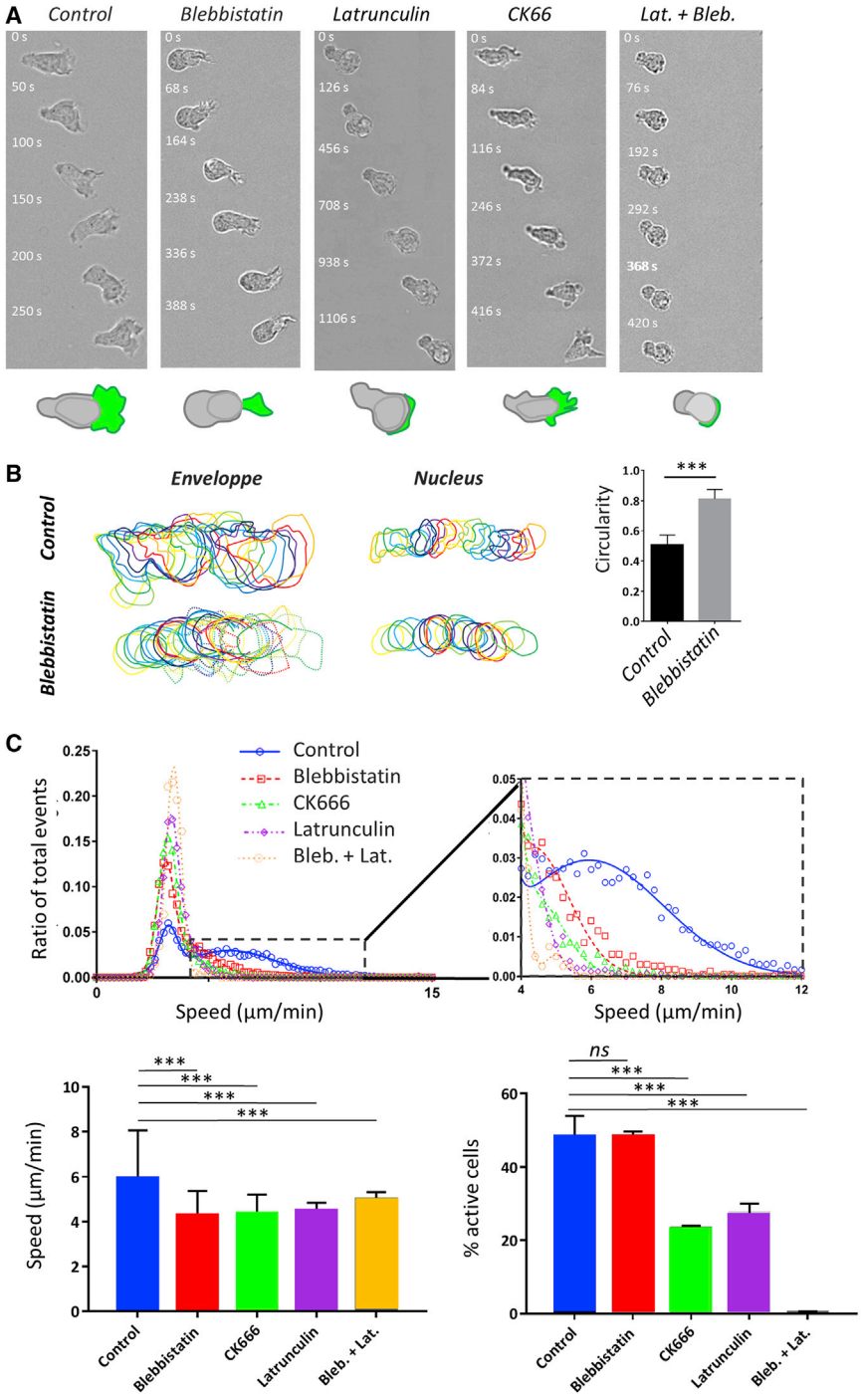

FIGURE 4 Actin propels swimming more by polymerization than by contractility. (*A*) Bright-field image sequences show the shape and dynamics of cells swimming on an antiadhesive substrate versus the addition of actomyosin inhibitors. Shown from left to right: wild-type cells and cells treated with 50 μM blebbistatin, 0.05 μM latrunculin, 100 μM CK666, and combined latrunculin and blebbistatin. See also Video S6. Cartoons at the bottom reproduce the cell in the first image to illustrate in each case the shape of the cell body (rear and nucleus) in gray and of the cell front or lamellipod in green. Blebbistatin-treated cells have a roundish cell body without traveling protrusion and a reduced but active lamellipod; latrunculin-treated cells have almost no lamellipod; and CK666-treated cells have a perturbed lamellipod forming blebs and spikes. Cells treated with blebbistatin and latruculin have a roundish noncontractile cell body and no lamellipod (Scale bars, 10 μm). (*B*) Left: shown are representative sequences of envelope and nucleus contours of a control cell (*top*) and of a cell treated with 50 μM blebbistatin (*bottom*), suggesting a difference of contractile activity. Time lag between each contour is 10 s. Right: shown is the quantification of the circularity of cells envelops for control cells and 50 μM blebbistatin treatment on image sequence taken at magnification $\times$60 and cell contour determined using Ilastik. Error bars correspond to standard deviation. Cells $N > 10$, and experiments $N = 3$. $^{***}p < 0.001$ (two-tailed Student's *t*-test). (*C*) Top: shown is a histogram of raw curvilinear speeds for swimming cells in response to abovementioned actin inhibitors treatments. The lines correspond to a fit by a double Gaussian function. Insert presents a zoom of the histogram for the active cells corresponding to the Gaussian of high mean speed. Bottom left: shown is the average speed and SD corresponding to the Gaussian of high mean speed. Bottom right: shown is the percentage of active motile cells, and error bars correspond to SEM. Cells $N = 4342$ (HBSS), 2353 (blebbistatin), 5582 (CK666), 2255 (latrunculin), and 403 (blebbistatin plus latrunculin). Error bars correspond to SEM. Experiments $N > 5$. $^{***}p < 0.001$ with respect to homogeneous substrate, one-way ANOVA followed by the Tukey multiple comparison test. To see this figure in color, go online.

and S5 and S6; Video S9). Our model presents the rare advantage of using only parameters accessible experimentally, such as the amplitude and speed of deformation waves. Waves of a few microns amplitude and 10 μm min^{-1} speed observed experimentally yielded in our simulation a swimming speed 1000 times slower than the experimental swimming speed (Fig. S7). This quantitative analysis suggests strongly that deformations are not efficient enough to propel swimming of lymphocytes. To support this result further, we performed perturbations of cell shapes by osmotic swelling. The addition of 50% of water in medium resulted in an average cell volume increase by 65%, as assessed by the size increase of round cells, and imposed a more roundish shape on motile cells, as assessed by the increase of their circularity index (Fig. 5 *C*; Video S10). Nevertheless, swimming speed was not significantly affected. This result

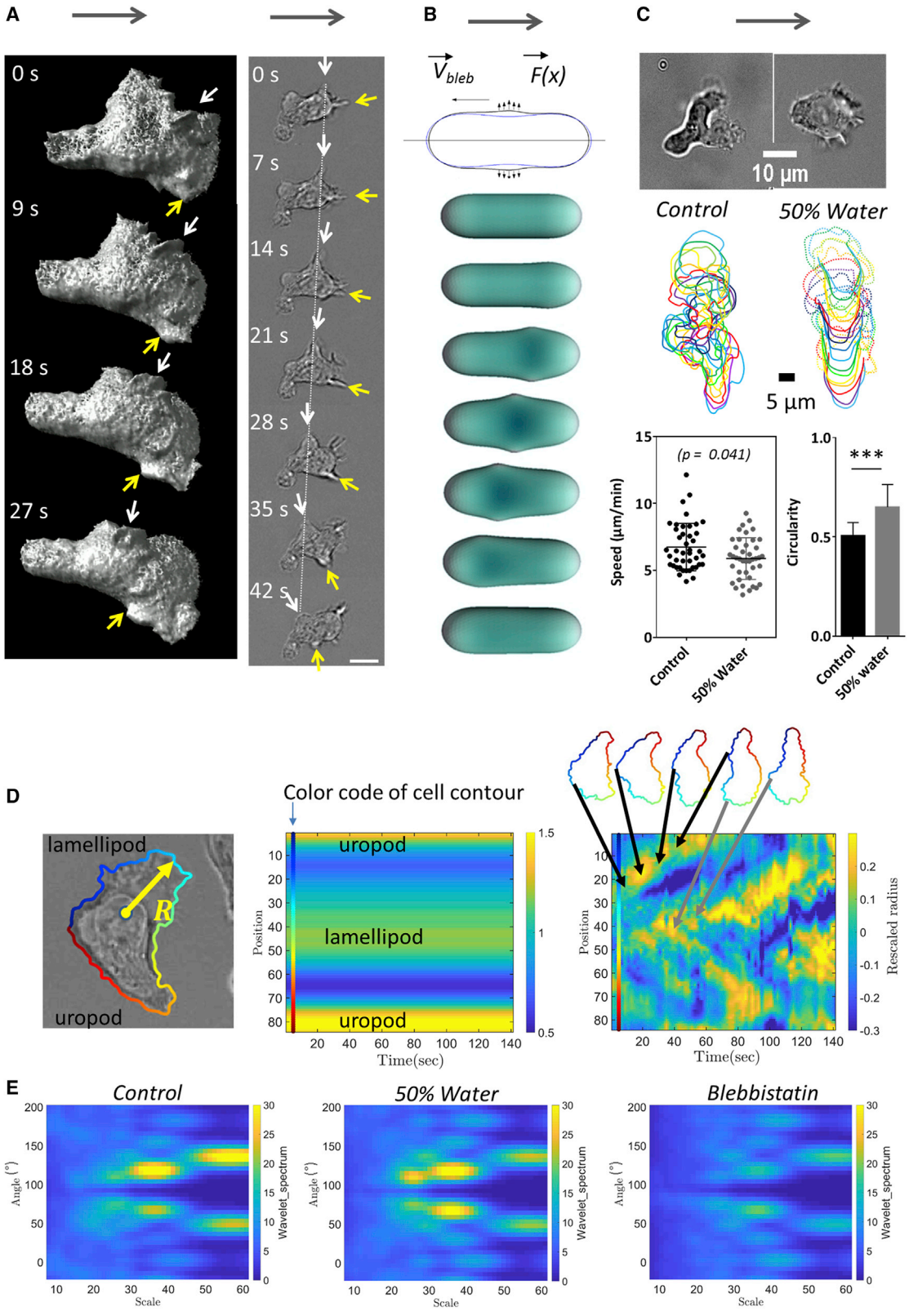

FIGURE 5 Protrusion paddling alone seems not efficient enough to propel swimming. (*A*) Image sequence of swimming cell with micron-scale protrusions traveling along cell body. Left: soSPIM images of a cell transfected with RFP-Lifeact reveals the shape and motion of waves of actin protrusion in three dimensions. White and yellow arrows point to particular protrusions. See also Video S7. Right: bright-field images of a swimming cell show dynamics of protrusions. See also Video S8. Protrusions (*white* and *yellow arrows*) travel backward in the frame of the cell and of the lab (*white dashed line*).

(legend continued on next page)

supports that average shapes are not crucial for swimming, but it says nothing about the role of propagating deformations. We then performed a spatiotemporal analysis of cell's contours using wavelet transforms (Figs. 5, *D* and *E*, S8, and S9). As compared to control cells, the dynamic mode of protrusion that propagated backward was found hardly altered by osmotic swelling but strongly affected by blebbistatin treatment. For osmotic swelling, protrusions paddling and swimming are both hardly perturbed, which yields little information. In contrast, with blebbistatin treatment, the amplitude of propagative protrusions was decreased by a factor larger than two (see also Video S6) so that swimming speed should decrease by more than 80% according to our model of propulsion by deformations (see Fig. S7). In fact, the experimental speed decreased by less than 25%, which further supports that protrusion may not be the main propelling source of swimming. Finally, we reasoned that if micron-scale deformations were not sufficient to propel swimming, sub-micron-scale deformations, typically undetected by optical microscopy, might mediate efficient propulsion. We therefore simulated the effect of submicronic waves by varying their number, shapes, and organization and found an optimum for an idealized case of trains of three waves traveling in phase (see Figs. S10 and S11). Still, swimming speed was more than 10 times slower than the protrusions traveling backward at 10 μm min^{-1}. Altogether, quantitative analysis and perturbations experiments support that cell deformations are not sufficient to propel lymphocytes swimming. This conclusion motivates the search of alternative and more plausible sources of propulsion.

Membrane rearward treadmilling correlates with swimming speed

Normal motion of cell membrane seems to yield insufficient propulsion, but the membrane of amoeboid cells displays also tangential movement triggered by the retrograde flow of the inner actin cortex. To evidence the motion of cell's external membrane, we incubated swimming cells with ICAM-1-coated beads. When cells encountered beads along their path, beads attached to the cell front via the transmembrane integrins LFA-1 and were carried backward (Fig. 6 *A*; Video S11). The average speed of beads in the reference frame of the cell was 12 $\pm$ 3 μm min^{-1}, which is significantly larger than swimming speed. Similar measurements with inhibitors blebbistatin, CK666, and latrunculin showed a decrease of bead's speed as compared to control (Fig. 6 *B*; Video S11). More precisely, the speed changes with blebbistatin, CK666, and latrunculin correlated with the respective changes in swimming speed (Fig. 6 *B*), which suggests a direct role of tangential membrane motion in swimming.

Retrograde flow of cell membrane can propel swimming

To analyze quantitatively the propulsion strength induced by tangential movements of the cell's membrane, we developed a basic model of retrograde flow, taking into account an internal actin cortex, a cytoplasmic lipidic membrane, and transmembrane proteins protruding outside the cell (Fig. 6 *C*). The transfer of movement from the inner cortex to the fluid surrounding the cell can be either total or partial depending on the coupling mechanism between the actin cortex and the lipids and proteins of the membrane, as discussed below. We first considered that the cell surface was made of a homogeneous membrane with an average treadmilling velocity proportional to the velocity of the actin cortex, v_a, and a transmission coefficient denoted β. In the laboratory frame, the velocity of the fluid adjacent to the cell membrane, denoted as v_f, is:

$$v_f(r) = \beta v_a(r) + v_s + \omega_s r, \tag{2}$$

where v_s and ω_s are, respectively, the translation and rotation swimming velocities of the cell. They were obtained by solving the Stokes equations (see Supporting Materials and Methods) in the fluid outside the cell, taking as boundary conditions that the flow vanished at large distances away from the cell and that it obeyed Eq. 2 at the cell surface. The obtained flow field was parametrized by the still unknown quantities v_s and ω_s, which allowed us to express the viscous

Gray arrows indicate swimming direction. Scale bars, 10 μm. (*B*) Schematic illustrates the model of cell swimming by protrusive blebs. Top: blue and black contours are the initial and deformed configurations of the cell in the model. Bottom: shown is the sequence of cell shapes obtained by the numerical simulation. Simulations yield that a cell propelled by shape waves is 1000 times slower than the protrusion wave (details in Supporting Materials and Methods). (*C*) Osmotic swelling affects cell shape but not swimming speed. Top: representative images of a cell in medium and in water dilution at 50%. Middle: representative cell contour sequences (time lag is 10 s between each contour). The cell swollen by osmotic stress displays less deformations of cell body (*full lines*), but lamellipod protrusions are still distinguishable (*dotted line*). Bottom: shown is the swimming speed in medium and with water dilution at 50%. (cells $N > 30$, p value of t-test) and circularity of cells on image taken at magnification $\times 60$, with cell contours determined using Ilastik. Error bars stand for standard deviation Cell $N > 10$, and experiments $N = 3$. $^{***}p < 0.001$ (two-tailed Student's t-test). See also Video S10. (*D*) Measurement of cell protrusion dynamics. Left: Shown is a representative example of an elliptic Fourier contour reconstruction. Radius R definition of edge distance to the center of mass is shown. Middle and right: shown are kymographs of rescaled R versus position along the cell perimeter, either averaged in time (*middle*) or with time-average contribution subtracted (*right*). Color scale on the left corresponds to the color code used in contour reconstruction, allowing one to identify the position in kymographs of lamellipod, uropod, and propagating protrusions. See also Fig. S8. (*E*) Spatiotemporal spectrum of protrusion dynamics by wavelet transform. Shown is the average wavelet spectra of rescaled R kymographs without time-averaged contribution (see also Fig. S9). To see this figure in color, go online.

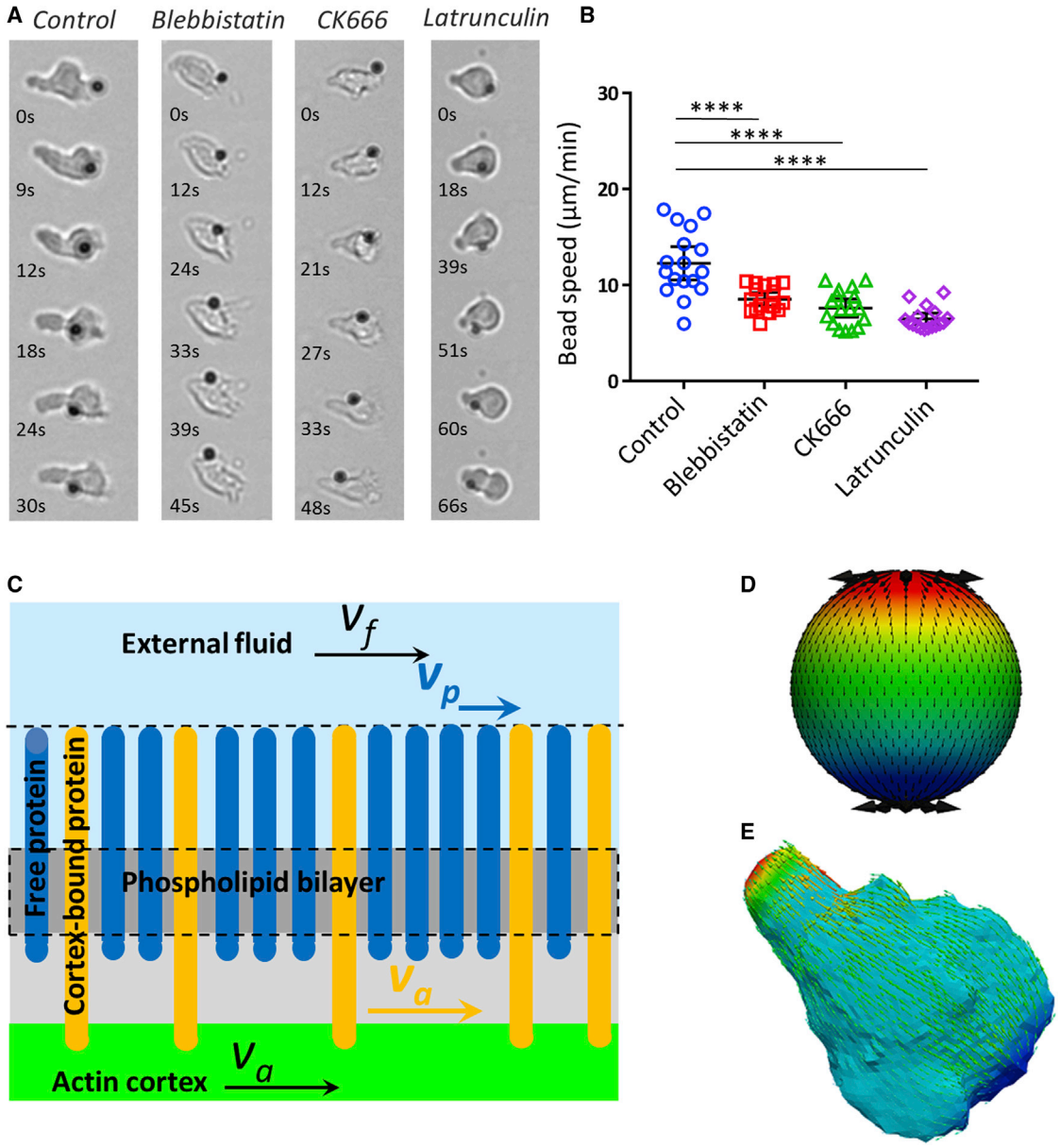

FIGURE 6 External membrane retrograde flow can propel swimming efficiently. (*A*) Bright-field images of ICAM-coated beads traveling from front to back on the cell membrane of swimming primary human effector T cells in HBSS control media and with 50 μM blebbistatin, 100 μM CK666, and 0.05 μM latrunculin (*left* to *right*). Scale bars, 10 μm. See also Video S11. (*B*) Traveling speed of ICAM-coated beads versus inhibitor type ($n = 17$ cells for each case, error bar is SD, ****$p < 0.0001$, Dunnet's multiple comparison test versus control condition). (*C*) Cartoon of the external and internal structure of the cell membrane considered in the modeling of membrane dynamics. (*D* and *E*) Retrograde flow pattern on a model spherical cell (*D*) and a cell with an experimental shape (*E*) extracted from soSPIM images of (Fig. 5 *A*). Swimming speed is found in both cases equal to the speed of the membrane at equator. See also Video S12. To see this figure in color, go online.

forces acting on the cell. The system was closed by imposing that the total force and torque acting on the swimmer vanished, yielding the values of v_s and ω_s. A remarkable observation is that the swimming velocity does not depend on the viscosity of the suspending medium for a given cortex velocity (see Supporting Materials and Methods for a proof), which is consistent with experimental observations. The problem could be solved analytically for a sphere (Fig. 6 *D*), and the swimming velocity was given by $v_s = \beta v_0$, where $v_0$is the retrograde flow velocity at the equator. β is found equal to 1 for a complete transmission between actin retrograde flow and external membrane. A similar result has been obtained by Lighthill for a model-ciliated swimmer (squirmer), which yielded $v_s = 2/3 v_0$ for the swimming speed (48), the difference of proportionality coefficient being due to the choice of the surface flow. For other shapes, we solved numerically the problem using the boundary integral formulation for the Stokes equations

(see Supporting Materials and Methods). In particular, we discretized a shape of T lymphocyte obtained by 3D soSPIM microscopy (Fig. 6 *E*) and introduced an actin source in a small region at the front of the cell and an actin sink at its rear. The overall flow pattern was similar to the spherical case, and the swimming velocity was close to the velocity of the cell membrane in the central region of the cell (in the cell frame), like for a spherical shape (Video S12). Besides, because most experimental data were obtained for cells close to a rigid wall, we used our numerical simulations to confirm that the swimming velocity was largely insensitive to the distance to the wall (see Fig. S12). Altogether, modeling confirms that swimming speed has the same magnitude as the speed of the external membrane treadmilling, supporting that cortex retrograde flow contributes significantly to lymphocyte swimming and could be the sole propelling source.

Membrane treadmilling is heterogeneous at the molecular scale

The propulsion model by a treadmilling membrane was considered a total coupling between the external fluid and a homogeneous membrane. This model yielded equal speeds between cell swimming and membrane treadmilling; however, the swimming speed ($v_s \sim 5\ \mu m\ min^{-1}$) was found two times smaller than the membrane treadmilling speed ($>10\ \mu m\ min^{-1}$) as revealed by beads attached to the membrane. This difference suggests that the coupling between cell membrane and surrounding fluid is not total and/or that the membrane is not homogeneous. Both the composition and the dynamics of a cell cytoplasmic membrane are indeed highly heterogeneous at a molecular level. The external fluid is therefore in contact with numerous lipids and transmembrane proteins and the hydrodynamic coupling between a fluid and such a complex surface is a delicate and hardly considered problem. Also, the molecular dynamics of the cell membrane itself is not fully characterized. If the retrograde flow of actin cortex and actin-bound transmembrane proteins is well attested, the circulation of lipids and of nonactin-bound transmembrane proteins is less documented. To get more insight into the molecular dynamics of the cell membrane at the timescale of tens of seconds and at the spatial scale of the entire cell, which are the relevant scales for cell swimming, we performed live FRAP-TIRF measurements on nonadherent cells maintained in the vicinity of the probing glass/fluid interface using depletion force induced by the addition of dextran in the medium. On RFP-actin-transfected cells, we observed the motion of actin clusters that displayed no detectable diffusion. The actin cortical cytoskeleton behaved like a solid gel (Fig. 7 *A*; Videos S13 and S14) flowing backward at $24 \pm 9\ \mu m\ min^{-1}$ (Fig. 7 *E*). This result for human lymphocytes is in the top range of literature for other cellular systems (between 6 and 20 $\mu m\ min^{-1}$) (12,19,34,49,50). For transmembrane proteins, different dynamics could be expected whether proteins could bind or not to the actin cortex. To shed light on this issue, we used fluorescent-specific antibodies against an actin-bound protein, the integrin LFA-1 in high affinity state, and a nonactin-bound protein, the ligand of T lymphocyte receptor, MHC-1. Like actin, actin-bound proteins LFA-1 formed clusters that persistently flowed backward (Fig. 7 *B*; Video S13) with an average speed of $25 \pm 5\ \mu m\ min^{-1}$ (Fig. 7 *E*). The absence of diffusion and similarity of speed with actin retrograde flow are consistent with a strong attachment rate of high affinity integrins to subcortical actin. By contrast, nonactin-bound proteins MHC-1 displayed a diffusive dynamics in FRAP experiments (Fig. 7 *C*; Video S13) with a characteristic diffusion coefficient of $D = 0.26 \pm 0.22\ \mu m^2\ s^{-1}$ (Fig. 7 *E*). Similarly, for the lipidic layer, FRAP experiments with Vybrant DiO lypophilic molecules inserted in the cytoplasmic membrane (Fig. 7 *D* and Video S13) yielded a diffusion coefficient of $3.1 \pm 1.8\ \mu m^2\ s^{-1}$ (Fig. 7 *E*). Altogether, these results confirm that the molecular dynamics of the plasma membrane is heterogeneous. Actin-bound transmembrane proteins display ballistic backward motion, whereas lipids and nonactin-bound transmembrane display diffusion. This heterogeneity was not taken into account in simulations and may explain the difference between the speed of cell swimming and actin treadmilling.

Model of retrograde flow transmission by a heterogeneous membrane

To quantify the effect of partial coupling between the actin retrograde flow and the external fluid through a heterogeneous membrane, we considered the layers of transmembrane proteins protruding in the external fluid as a brush of polymeric molecules and analyzed the flow inside the brush composed of either advected or diffusing molecules. Based on polymer science developments, the brush of proteins was considered as a Brinkman medium (51) with a hydrodynamic penetration length, denoted as $\lambda^{-1} \sim r/[2(\varphi_i^{2D})^{1/2}]$, where φ_i^{2D} is the area fraction occupied by advected transmembrane proteins (e.g., integrins), and r is the typical lateral extent of the proteins on the membrane. The transmission coefficient can be expressed as:

$$\beta = 1 - 2g/(1+g^2) \quad with \quad g = e^{\lambda h}, \tag{3}$$

where h is the brush thickness. We first considered the effect of advected proteins linked to actin. Integrins LFA-1 and VLA-4, dominant in lymphocytes, were measured with an average occurrence of 25,000 and 15,000 molecules per cell, respectively (Fig. S13). Considering a radius $r = 5$ nm for each integrin and an excess of membrane in microvilli of 150%, the surface occupancy of LFA-1/VLA-4 corresponds to a mere 0.1%. The fact that integrins are not in

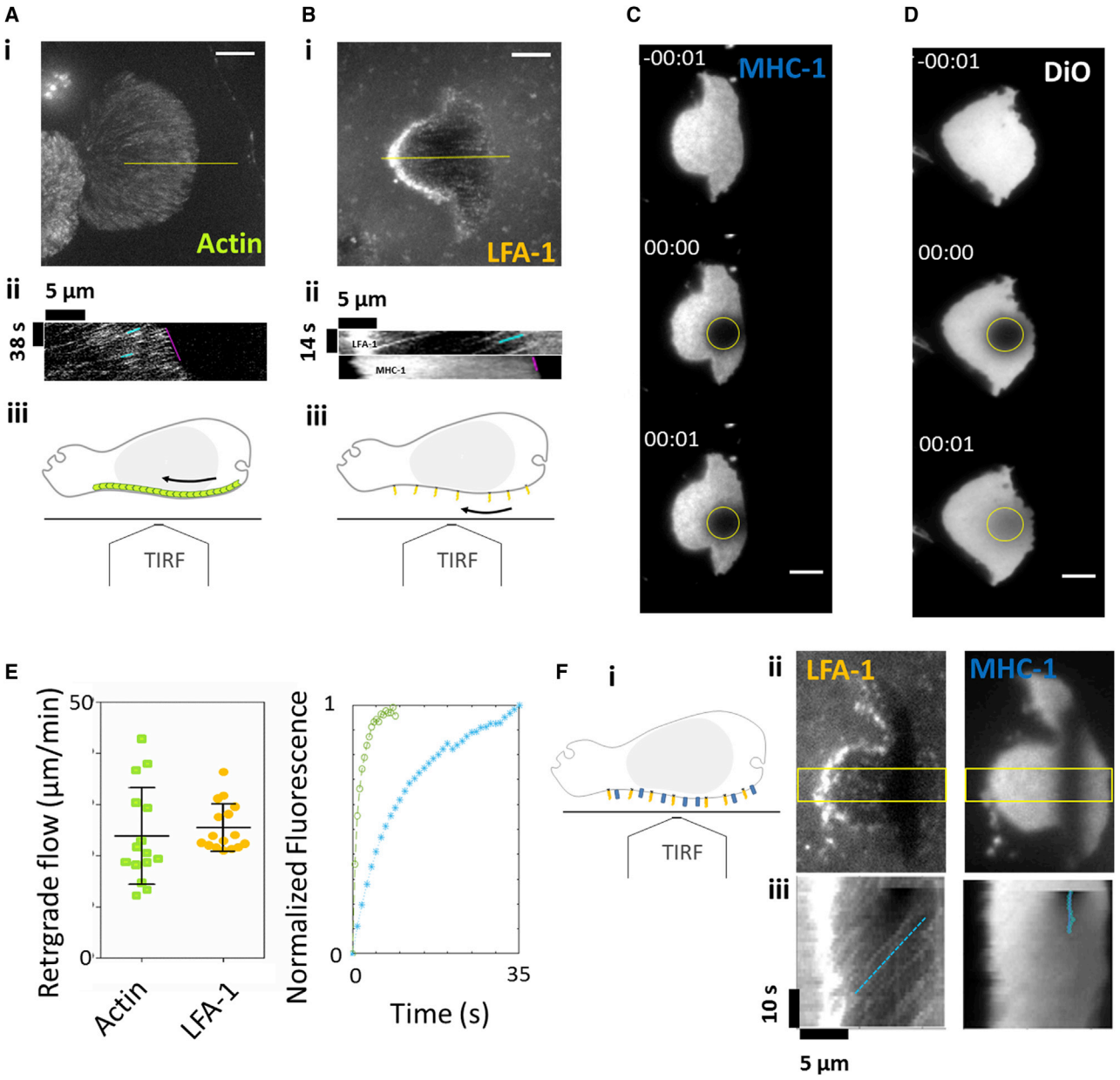

FIGURE 7 Actin-bound proteins LFA-1 treadmill backward at the cytoplasmic membrane, whereas nonactin-bound protein MHC-1 diffuses without net transport. (*A* and *B*) Backward transports of actin and actin-bound LFA-1 transmembrane protein are shown. (*i*) Maximal intensity projection of TIRF sequences on adhesion-free cells transduced with RFP-actin (*A*) and stained with antibody M24 that binds the actin-bound integrin LFA-1 in its high-affinity state (*B*). Scale bars, 5 μm. (*ii*) Representative kymographs along the yellow line in (*i*), with the front advance highlighted in magenta and clusters retrograde flow highlighted in blue. See also Videos S13 and S14. (*iii*) Schematics representing a side view of a nonadherent cell observed with a TIRF objective and highlighting the retrograde flow of internal actin (*green units*) and external LFA-1 integrins (*orange bars*). (*C* and *D*) Diffusive dynamics of nonactin-bound transmembrane protein MHC-1 and lipidic DiO marker. TIRF-FRAP experiments on adhesion-free cells (*C*), stained with anti-HLA-ABC that binds the nonactin-bound MHC-1 type I proteins and (*D*) with membrane lipidic marker DiO. Yellow circles indicate frapped regions used to calculate fluorescence recovery. Scale bars, 5 μm. (*E*) Quantification of transmembrane proteins advection and diffusion. Left: speed values for retrograding actin were measured by cluster tracking as in (*D*) ($n = 7$ cells, 51 clusters tracked) and by FRAP as in Supporting Materials and Methods ($n = 8$ cells) and for LFA-1 clusters ($n = 16$ cells, 106 clusters tracked), all normalized to the front of the cell. Error bars stand for standard deviation. Right: shown are the averaged FRAP curves for DiO (*blue*, $n = 10$ cells) and MHC-1 (*green*, $n = 14$ cells). All values were normalized and corrected by a nonbleached cell. Diffusion coefficient is of 3.1 $\pm$ 1.8 μm^2/s for DiO and 0.26 $\pm$ 0.22 μm^2/s for MHC-1. (*F*) Single cell evidence of average backward advection for actin-bound LFA-1 and average absence of motion for nonactin-bound MHC-1. (*i*) Schematics representing a side view of a nonadherent cell double stained for LFA-1 (*orange*) and MHC (*blue*). (*ii*) TIRF images after FRAP bleaching of a line pattern reveal actin-bound activated LFA-1 in its high-affinity state (*left*) and nonactin-bound MHC-1 (*right*). (*iii*) Kymographs in the yellow rectangle in (*ii*) with the motion of clusters and the center of mass of the FRAP region highlighted in blue for, respectively, LFA-1 and MHC-1. See also Video S15. To see this figure in color, go online.

high-affinity state at the same time tends to decrease further this value. Conversely, T lymphocytes express other integrins and other transmembrane proteins that link actin (e.g., T cell receptor or CD44), which tends to increase the surface occupancy by advected molecules. All in all, exhaustive experimental data are lacking to determine the exact value of φ_i^{2D}. However, assuming φ_i^{2D} of 2% and h of 20 nm, the theoretical coupling value was found at $\beta = 0.2$, which is in agreement with the experimental result of a swimming speed five times smaller than the cortex retrograde flow. The effect of diffusing transmembrane proteins was also taken into account by considering that they were indirectly advected by the drag of the external fluid and by viscous interactions within the membrane. Modeling of fluid drag and estimation of membrane viscosity from FRAP measurements allowed us to show that membrane viscosity dominates over the external fluid drag (Supporting Materials and Methods) and that the presence of diffusing transmembrane proteins reduces the value of β (Fig. S14). Altogether, membrane treadmilling can participate in swimming, and heterogeneity of the membrane can significantly modulate the coupling efficiency.

Actin-bound proteins are advected backward at cell membrane, whereas nonactin-bound proteins are not

Simulations show that swimming speed decreases when a fraction of cell membrane has no backward motion. Assessing the average motion of lipids was not possible experimentally because of their fast diffusion. However, for transmembrane proteins, we managed to get more insight by performing line-shaped FRAP experiments on cells with double staining for LFA-1 and MHC-1. On Fig. 7 *F*, clusters of LFA-1 and the center of mass of the FRAP zone for LFA-1 moved backward at 22 μm min^{-1}, in line with previous measurements. In contrast, the center of mass of the FRAP zone for diffusing MHC-1 was on average immobile. These data are a direct support that a fraction of the membrane is purely diffusive and hinders the propulsion effect of paddling molecules.

Actin-bound proteins are recycled by internal vesicular extrusion and nonactin-bound proteins are not

A sustainable retrograde flow at the surface of an axisymmetric object requires a source of material at the front and a sink at the back, which therefore implies the existence of an internal anterograde transport to loop a cycle. Conversely, when molecules are not advected backward (and are only diffusive), there must be no internal frontward recycling because a source at the cell front would generate an external retrograde flow. Our swimming model implies therefore the existence and the absence of an internal anterograde recycling of, respectively, actin-bound and nonactin-bound proteins. To support further the relevance and consistency of our model, we then intended to verify these two properties by performing square-shaped FRAP experiments on the cell front (Fig. 8 *A*; Video S16). In the case of LFA-1, a source of fluorescence at the cell leading edge after photobleaching (Fig. 8 *A*; Video S16) was consistent with the extrusion of integrins originated from the unbleached cell rear and carried undetected by TIRF by internal vesicular transport. Interestingly, the cycle of extrusion/treadmilling of integrins occurred within a minute, which is consistent with the treadmilling and swimming timescales. These observations validate the existence of a complete cycling of integrins by treadmilling and vesicular transport, whose timescale is consistent with swimming speed. In the case of MHC-1, fluorescence after photobleaching recovered only by diffusion from the cell back (Fig. 8 *B*; Video S16), and there was no source at the cell front. This confirms that internal recycling is not occurring for this nonactin-binding protein. Altogether, FRAP-TIRF data support that lymphocyte membrane does not treadmill as a whole. Actin-bound proteins undergo retrograde ballistic motion externally and anterograde vesicular transport internally, whereas nonactin-bound proteins undergo diffusion at the cell surface without internal recycling. Some surface molecules treadmill and paddle, whereas others diffuse and hinder motion.

Treadmilling of a heterogeneous membrane can propel ubiquitous locomotion

Cell swimming by molecular paddling of a heterogeneous membrane is illustrated in Fig. 9 *A* with the treadmilling proteins exerting propulsion (*orange*), the diffusing proteins hindering propulsion (*blue*), and the inner recycling of paddling proteins by vesicular transport. To test further the mechanism, we perturbed the molecular cycling machinery without affecting actin treadmilling or actin-driven cell deformations by using inhibitors of endocytosis. Fig. 9 *B* shows results with primaquine 100 μM (52) and with a cocktail of inhibitors, including a clathrin inhibitor (pitstop2 50 μM), a dynamin inhibitor (dynasore 200 μM), and an inhibitor of the Arf6 GEF cytohesin (secinH3 20 μM) (28). Swimming was significantly slowed down with doses low enough to preserve cell morphological dynamics. The fact that osmotic swelling did not affect swimming speed (Fig. 5) is consistent with heterogeneous treadmilling propulsion because swelling does not affect protein cycle, and cell shape has a marginal influence on propulsion by treadmilling (Fig. 6, *E* and *D*). Beyond swimming, it is interesting to underline that the heterogeneous treadmilling mechanism can also foster propulsion on adherent 2D substrates and 3D matrices coated with integrin ligands. In these cases, the integrin-mediated clutch mechanism promotes optimal momentum transfer between

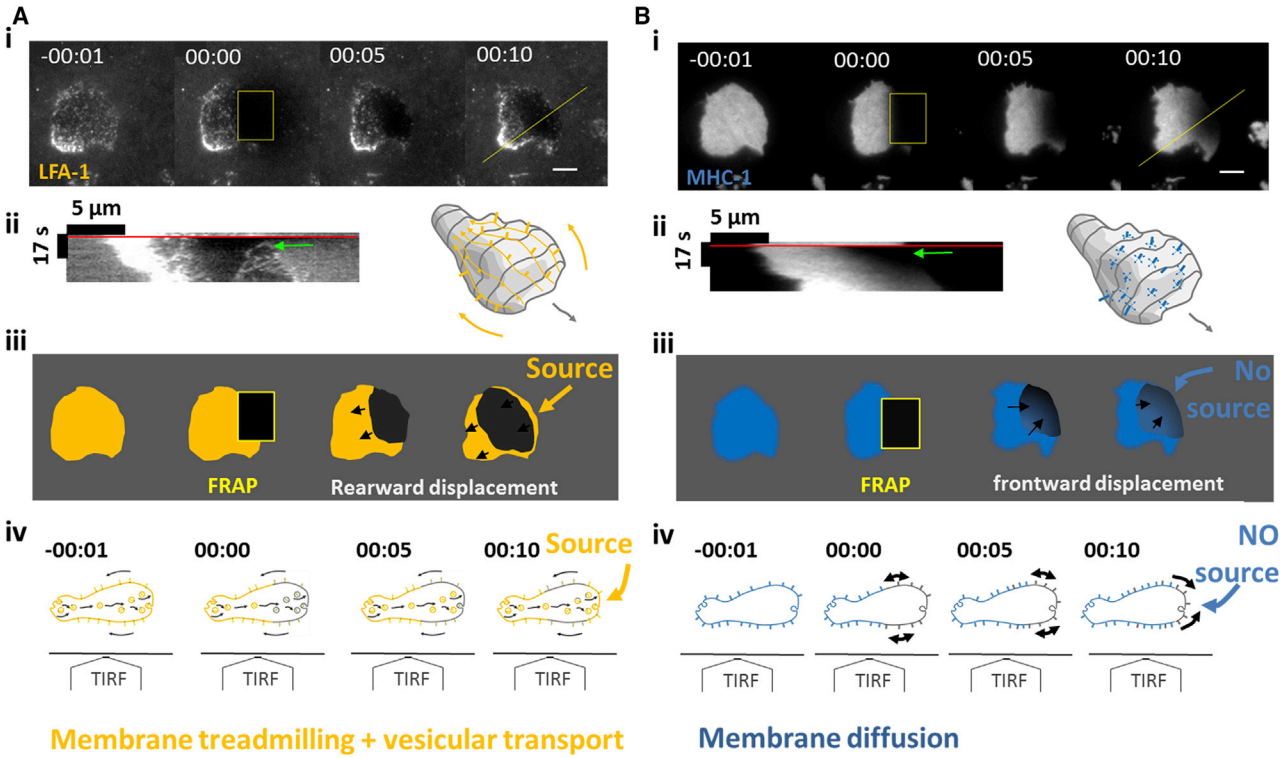

FIGURE 8 Treadmilling actin-bound transmembrane protein LFA-1 is recycled by internal vesicular transport, whereas diffusive transmembrane protein MHC-1 is not. (*A*) Staining of high affinity LFA-1 and (*B*) of MHC-1. (*i*) Sequences of TIRF images before FRAP, after FRAP of cell leading edge, and then 5 and 10 s after FRAP. Scale bars, 5 μm. See also Video S16. (*ii*) Kymographs along yellow lines of figures (*A* and *B*), with red lines indicating FRAP time and green arrows pointing at the cell front shortly after FRAP. 3D cartoon illustrates backward treadmilling of LFA-1 and 2D diffusion of MHC-1. (*iii*) Schematics of experimental results in (*i*) illustrate that fluorescence recovers from the cell leading edge for LFA-1, revealing a source at cell front, and from the back for MHC-1, revealing the absence of source at cell front. (*iv*) Side view schematics of nonadherent cells observed with a TIRF objective illustrate the dynamics of transmembrane proteins evidenced in TIRF experiments. For actin-binding LFA-1, the source at cell front reveals internal frontward transport of fresh material exocytosed at cell front, whereas for nonactin-binding MHC-1, purely diffusive transport dominates. To see this figure in color, go online.

internal cortex and external medium, and cell speed is indeed close to actin treadmilling speed. This corresponds to actin-integrin clutch mechanism (10). Furthermore, the heterogeneous treadmilling mechanism can also propel cells through nonadherent confined environments because friction of the cell membrane with a solid substrate is expected to be stronger than with a fluid. We found that cells confined between two plates and in microfluidic tubes were motile (Fig. 9 *C*; Videos S17 and 18). Between plates, two adjacent zones with adherent and nonadherent coatings were prepared by optical patterning (43), and tube surfaces were treated with Pluronic F107 (14). Cells are slightly faster between plates and significantly faster in tubes as compared to swimming mode. Literature data reported the case of cells in a microfluidic channel displaying treadmilling of membrane but no motion, which was interpreted as an example of null friction and null transmission between membrane and substrate (14). However, an ideal solid/cell interface with perfect slippage or null friction is not physically relevant because hydrodynamics of physical contact always yield friction. The mechanism of heterogeneous membrane treadmilling supports therefore ubiquitous lymphocyte migration in fluid and solids, with and without adhesion.

DISCUSSION

Amoeboid migration of mammalian cells, i.e., leukocytes and cancer cells, has attracted intensive interest in the last decade for their ubiquitous ability to migrate at high speed in various 2D and 3D environments. The requirement of adhesion with a substrate remains a widely accepted hallmark for 2D migration (5–7,12,14–19), whereas two studies reported nonadherent motility and swimming with leukocytes (20,28). However, Barry and Bretscher (20) did not investigate the mechanisms of neutrophils swimming, and O'Neil et al. (28) considered an original but artificial swimming mode induced by optogenetic activation of contractility in the cell rear. In this context, we provided here direct experimental evidences and quantifications of swimming by primary lymphocytes, together with an original theoretical model of molecular paddling that can explain amoeboid swimming at speeds compatible with precise

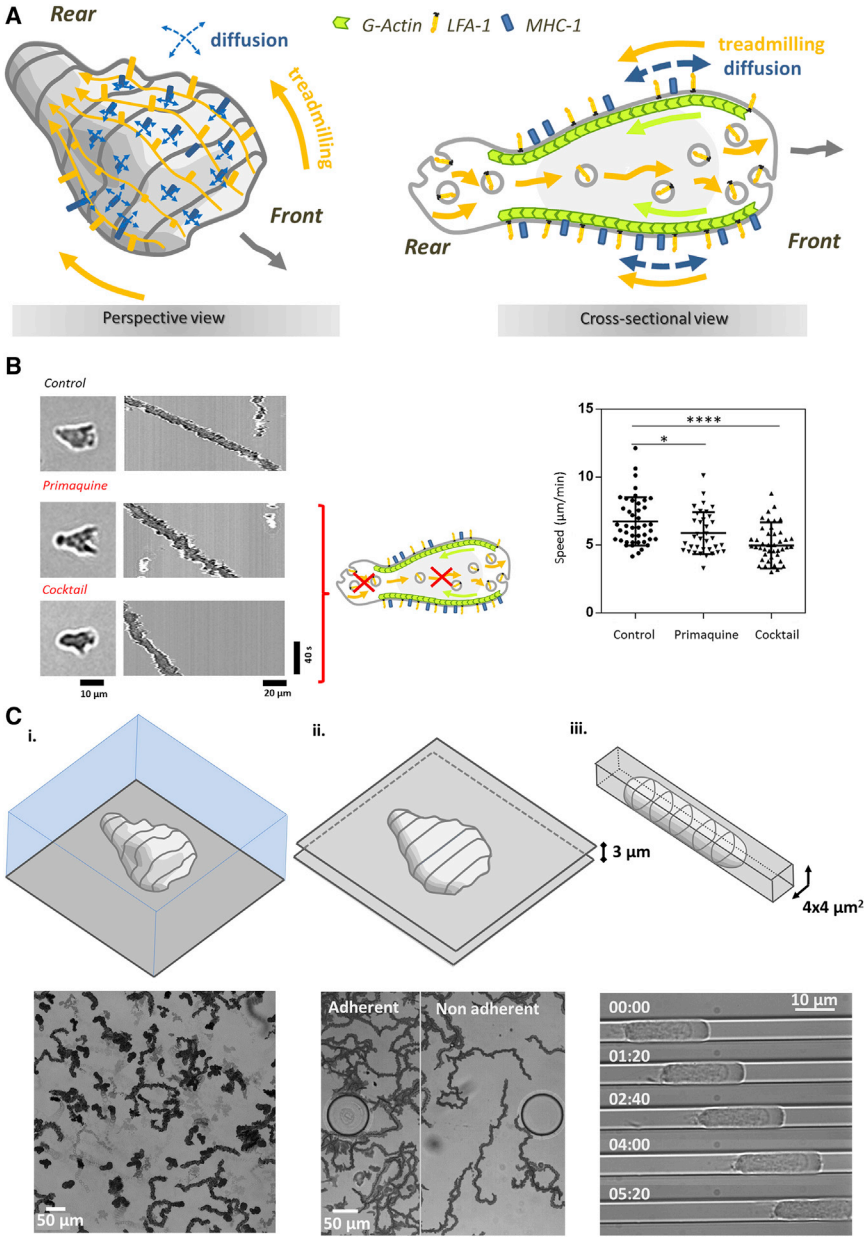

FIGURE 9 Treadmilling of transmembrane proteins recycled from rear to front by internal transport provides ubiquitous propulsion. (*A*) Schematics of heterogeneous membrane treadmilling mechanism. The perspective view displays a swimming cell on which actin-bound proteins (*orange*) are advected backward and entangled with nonactin-bound proteins. Swimming is promoted by advected proteins and hindered by diffusing proteins, which results in swimming significantly slower than treadmilling. The cross-sectional view displays the complete cycling of actin-binding proteins (*orange*), which comprises endocytosis at cell rear, internal advection by vesicles forward, exocytosis at cell front, and advection at cell membrane backward by linkage to retrograde actin flow (*green*). (*B*) Specific perturbation of paddling cycle by inhibitors of endocytosis (cartoon). Left: shown are representative images of a cell; middle: shown are representative kymographs of the swimming motion of the corresponding cells; and right: shown is a plot of the raw curvilinear swimming speeds for control conditions, with primaquine at 100 μM and with a cocktail of inhibitors (pitstop2 at 50 μM, dynasore at 200 μM, and secinH3 at 20 μM). $N = 30$ cells, *p < 0.05 and ****p < 0.0001 (two-tailed Student's t-test). (*C*) Heterogeneous treadmilling fosters ubiquitous motility without adhesion. (*i*) Swimming on a nonadherent surface, (*ii*) crawling between two surfaces separated by 3 μm, with adherent and nonadherent zones (see also Video S17), and (*iii*) in a nonadherent tube of cross section 4×4 μm^2 (see also Video S18). Data for cases (*i*) and (*ii*) correspond to projected images taken every 10 s for 3 min of a given area with several cells. The round shapes in (*ii*) correspond to 100-μm diameter glass pillars that sustain the structure. Data for case (*iii*) show a sequence of images of a single cell for 5 min. To see this figure in color, go online.

experimental measurements as well as ubiquitous migration in/on adherent and nonadherent substrates.

In principle, cell swimming without flagella can be propelled either by normal (protrusion) and/or tangential (treadmilling) motion of the cell membrane. Mechanistic studies of swimming by eukaryotic cells have mostly focused on amoeba *D. discoideum* and favored propulsion by shape deformation rather than treadmilling (21,24–26). However, most models involve parameters difficult to link to experimental data (26) or yield a swimming speed smaller than the experimental ones (24,25). There is therefore no consensus for swimming propelled by deformation. Interestingly, a recent study by O'Neil et al. (28) put forward original evidence that membrane treadmilling could be involved in propulsion, however without assessing the contributions of deformations in propulsion. Here, we proposed theoretical and experimental evidences that swimming of lymphocytes is barely relying on cell deformations. Modeling based only on parameters accessible experimentally like the micron-scale amplitudes and 10–20 μm min^{-1} speed of protrusions yielded that cell deformations cannot propel swimming at a speed as high as 5 μm min^{-1}. Experimental perturbations of the average and time-dependent cell deformations were also hardly perturbing swimming prowess. In contrast, experiments and modeling both validated a high efficiency of propulsion by membrane treadmilling, as proposed by O'Neil et al. (28), and we further show that membrane does not treadmill as a whole. Altogether, the

effect of shape deformations seems negligible in lymphocyte swimming, whereas membrane treadmilling would be the main propelling machinery.

Actin dynamics acts a priori as a hybrid motor of membrane treadmilling, polymerization at the cell front pushing the nascent cross-linked cortical network backward, and contractility at the cell rear pulling the network backward. It is not clear whether the two mechanisms combine their action on a continuous actin gel or if they act independently on disconnected actin networks at the cell front and rear. However, we found here that lymphocyte swimming relies more on frontal actin polymerization than on rear myosin II contractility. This diverges from the Rho-A-induced swimming mode described by O'Neil et al. (28) as well as from several recent reports on adherent crawling (15,18,53–57) that attribute a dominant propelling role to a gradient of contractility along cell's front-rear polarization axis. Our results are more in line with studies proposing that contractility is marginally involved in propulsion and mostly relevant for the detachment of cell rear (for *Dictyostelium* amoebae) (58) or for the squeezing of cell nucleus through pores (for dendritic cells) (5). Hence, depending on cell types, actin treadmilling may be powered more by actin network contractility (28) or by actin polymerization, but in any case, our results corroborate the idea that membrane treadmilling is an essential player of lymphocyte motility, either by swimming or crawling.

Hydrodynamic coupling between a treadmilling membrane and a surrounding fluid is the key of amoeboid swimming, and we analyzed here its molecular basis experimentally and theoretically. Studies considering that cellular membranes treadmill as a whole yield a theoretical ratio between swimming and membrane speeds ranging between 2/3 and 1 (59). O'Neil et al. (28) measured swimming speeds 2/3 of membrane speeds and observed gradients of several membrane components (lipids and proteins) along cell rear-front axis. This led them to conclude that the cell membrane was treadmilling as a whole and propelling swimming. One may, however, argue that their correlation between speeds of membrane and speed of cell swimming relied on a narrow set of data. Besides, proteins gradients do not strictly imply that proteins treadmill because gradients can also result from a balance between diffusion and drag by surrounding molecules. In contrast, the analysis of lymphocyte swimming motion showed here that swimming speed was 1/3 of membrane treadmilling speed (measured with a bead attached to the membrane) and 1/5 of the actin-bound proteins speed (measured by TIRF) and therefore too low to arise from the treadmilling of a homogeneous membrane. Moreover, direct microscopy experiments showed that membrane dynamics was heterogeneous at the molecular level and that only a fraction of transmembrane protein treadmilled backward. Hence, some membrane molecules treadmill backward, paddle, and promote swimming, whereas others are diffusive and hinder swimming. Simulations of propulsion by a heterogeneous treadmilling support further that a fraction of treadmilling proteins is efficient enough to support swimming at a speed close to internal cortex speed, and also that a fraction of diffusing protein can significantly slow down speed to the observed swimming speed.

Importantly, we also showed that treadmilling of actin and transmembrane proteins, whose essential role has been widely inferred in cell motility, was associated with sophisticated mechanisms of internal vesicular transport to sort proteins that support continuous swimming. Vesicular transport is indeed implemental to complete the cycle of paddling proteins and promote sustained propulsion, and the sorting of proteins transported by vesicles is also necessary to explain heterogeneity of proteins dynamics at cell surface. Internal transport of a treadmilling transmembrane protein and the absence of internal frontward recycling of a diffusion transmembrane protein was evidenced here by FRAP with, respectively, integrin LFA-1 and protein MHC. Mechanisms of internal integrins recycling by anterograde vesicular transport have also been documented in the literature (60–64). Moreover, the cycle of extrusion/treadmilling of integrins in our experiments occurred within a minute, which is in line with the treadmilling and swimming timescales (in contrast to literature data that reported timescales around 15–30 min (61,62)).

Our swimming model sheds also new light on the ubiquitous motility of amoeboid cells. The adaptation of mammalian amoeboid cells to various environments has repeatedly been attributed to their capability to switch between different migration modes versus the environment (10,14,15,19,33,57). The mode of adherent crawling is generally attributed to a sequence of cell front protrusion/attachment and cell rear pulling/detachment, whereas the more intriguing mode of nonadherent migration in 3D has been explained by various mechanisms depending on cell types (9,19): blebbing in the cell front and transfer of actin cytoskeleton into the novel bleb (54,65,66), intercalation of protrusion into gaps and discontinuities of the matrix to advance like on a ladder (67–69), chimneying via active gel pushing off the wall (11), cell rear contractility stabilizing a single bleb conformation (18), water permeation throughout the cell body (70), or treadmilling coupled to friction with the substrate (8,9,12). In our case, there was no evidence of a mode switching between crawling and swimming sequences on patterned substrates, and treadmilling of a heterogeneous membrane can propel ubiquitous migration of lymphocytes versus solid (8,12) or liquid environments. In this scheme, speed depends on cell/environment coupling conditions. An adhesive solid environment provides optimal coupling and cell's speed is close to actin treadmilling speed (unless detachment issues slow down motion); a liquid environment provides a minimal coupling due to the molecular heterogeneity of cell membrane treadmilling (the environment fluidity is not directly responsible

for weak coupling, as attested by our model or by the squirmer model (48)); and finally, a nonadherent confined environment provides an intermediate coupling, in which friction relies on surface forces rather than on hydrodynamic lubrication (40). The regime of hydrodynamic friction (or lubrication) appears, indeed, only for objects much faster than crawling cells (71). Interestingly, the propulsion by heterogeneous membrane treadmilling supports systematic migration in nonadherent confined environments because a solid/cell interface with null friction is not physically relevant. Furthermore, nonadherent confined propulsion is expected to be at least as fast as swimming because the coupling of the membrane with a solid can only be more efficient than with a liquid. Altogether, the mechanism of heterogeneous membrane treadmilling is operational in polarized cells displaying backward actin treadmilling. This mechanism can allow ubiquitous adaptation of lymphocytes to various microenvironments via a single mode of migration (10) associated to different friction/adhesion coupling conditions. It may exist for other cell types and coexist with other propulsion mechanisms.

In the end, heterogeneous membrane treadmilling can drive ubiquitous amoeboid migration within fluid and solid and with or without adhesion; however, the physiological role of swimming remains enigmatic for leukocytes. Because the traffic of immune cells (or invasivity of cancer cells) relies mostly on matrix-associated migration and because swimming is clearly relevant to planktonic eukaryotic cells (like amoeba), it is possible that the basic machinery for swimming is an evolutionary conserved ability that has found novel functions for ubiquitous crawling in mammalian cells. Nevertheless, swimming might be instrumental to extend the ubiquitous migration capabilities of immune cells to nonconfining conjunctive tissues or liquid-rich infected niches like postwound edema zones.

SUPPORTING MATERIAL

Supporting Material can be found online at https://doi.org/10.1016/j.bpj.2020.07.033.

AUTHOR CONTRIBUTIONS

L.A. and P.N. worked on all experiments and analysis except TIRF-FRAP section. A.F. developed all modeling and simulations on treadmilling mechanism and contributed to swimming speed analysis. N.G.-S. performed experiments of beads tracking and all FRAP-TIRF assays. M.S.R. performed modeling of shape deformation mechanism. X.L. performed migration assays on patterned substrates. S.T. performed elliptic Fourier reconstruction of contours and wavelet transforms. M.B.-P. managed cell culture, performed transfection with RFP-Lifeact, and made quantitative cytometry. M.-P.V. participated in experiments and analysis. R.G. and J.-B.S. performed 3D live imaging by soSPIM. C.H. and S.D. prepared GFP-actin cells. S.R. performed viscosity measurements and participated in discussions. C.M. supervised and participated in all modeling developments, designed the study, and wrote the article. O.T. supervised and participated in all experiments and analysis, designed the study, and wrote the article.

ACKNOWLEDGMENTS

We are grateful to Claire Chardes and Pierre-Francois Lenne for help with light-sheet imaging trials, and to Marc Bajenoff and Yannick Hammon for helpful discussions. C.M. and S.R. thank D.K. Dysthe for many valuable discussions and for having clarified several issues of the amoeboid swimming problem during his 1-year stay in LIPhy in 2011 as well as Alain Duperray and Nawal Quennouz for valuable discussions regarding their preliminary experiments on swimming of neutrophils.

The work at LAI was supported by the French Agence Nationale de la Recherche (RECRUTE ANR-15-CE15-0022 and ILIAAD ANR-18-CE09-0029), the LABEX INFORM, the Région Sud, the Turing Centre for Living systems, the Excellence Initiative of Aix-Marseille University – A*MIDEX, a French "Investissements d'Avenir" programme, and the company Alveole. We also thank the France Bioimaging Platform, funded by the French Agence Nationale de la Recherche (ANR–10–INBS–04–-01, Investments for the future). Authors also thank the electronic imaging center of Bordeaux Imaging Centre for metallization of the soSPIM chambers, the ANR grants soSPIM and soLIVE, the Cell Culture Platform facility (Luminy TPR2-INSERM, Marseille), and the National Infrastructure France BioImaging supported by the French National Research Agency (ANR-10-INBS-04). The work at LIPhy was supported by Centre National d'Etudes Spatiales, European Space Agency, and the French-German university programme "Living Fluids" (grant CFDA-Q1-14).

REFERENCES

1. Taylor, G. 1951. Analysis of the swimming of microscopic organisms. *Proc. R. Soc. Lond. Math. Phys. Eng. Sci.* 209:447–461.
2. Farutin, A., S. Rafaï, …, C. Misbah. 2013. Amoeboid swimming: a generic self-propulsion of cells in fluids by means of membrane deformations. *Phys. Rev. Lett.* 111:228102.
3. Abercrombie, M. 1980. The Croonian lecture, 1978: the crawling movement of metazoan cells. *Proc. R. Soc. Lond. B Biol. Sci.* 207:129–147.
4. Ridley, A. J., M. A. Schwartz, …, A. R. Horwitz. 2003. Cell migration: integrating signals from front to back. *Science.* 302:1704–1709.
5. Lämmermann, T., B. L. Bader, …, M. Sixt. 2008. Rapid leukocyte migration by integrin-independent flowing and squeezing. *Nature.* 453:51–55.
6. Malawista, S. E., and A. de Boisfleury Chevance. 1997. Random locomotion and chemotaxis of human blood polymorphonuclear leukocytes (PMN) in the presence of EDTA: PMN in close quarters require neither leukocyte integrins nor external divalent cations. *Proc. Natl. Acad. Sci. USA.* 94:11577–11582.
7. Malawista, S. E., A. de Boisfleury Chevance, and L. A. Boxer. 2000. Random locomotion and chemotaxis of human blood polymorphonuclear leukocytes from a patient with leukocyte adhesion deficiency-1: normal displacement in close quarters via chimneying. *Cell Motil. Cytoskeleton.* 46:183–189.
8. Hons, M., A. Kopf, …, M. Sixt. 2018. Chemokines and integrins independently tune actin flow and substrate friction during intranodal migration of T cells. *Nat. Immunol.* 19:606–616.
9. Paluch, E. K., I. M. Aspalter, and M. Sixt. 2016. Focal adhesion-independent cell migration. *Annu. Rev. Cell Dev. Biol.* 32:469–490.
10. Renkawitz, J., K. Schumann, …, M. Sixt. 2009. Adaptive force transmission in amoeboid cell migration. *Nat. Cell Biol.* 11:1438–1443.
11. Hawkins, R. J., M. Piel, …, R. Voituriez. 2009. Pushing off the walls: a mechanism of cell motility in confinement. *Phys. Rev. Lett.* 102:058103.
12. Bergert, M., A. Erzberger, …, E. K. Paluch. 2015. Force transmission during adhesion-independent migration. *Nat. Cell Biol.* 17:524–529.

13. Nourshargh, S., P. L. Hordijk, and M. Sixt. 2010. Breaching multiple barriers: leukocyte motility through venular walls and the interstitium. *Nat. Rev. Mol. Cell Biol.* 11:366–378.

14. Bergert, M., S. D. Chandradoss, …, E. Paluch. 2012. Cell mechanics control rapid transitions between blebs and lamellipodia during migration. *Proc. Natl. Acad. Sci. USA.* 109:14434–14439.

15. Jacobelli, J., F. C. Bennett, …, M. F. Krummel. 2009. Myosin-IIA and ICAM-1 regulate the interchange between two distinct modes of T cell migration. *J. Immunol.* 182:2041–2050.

16. Smith, A., Y. R. Carrasco, …, N. Hogg. 2005. A talin-dependent LFA-1 focal zone is formed by rapidly migrating T lymphocytes. *J. Cell Biol.* 170:141–151.

17. Friedl, P., and K. Wolf. 2010. Plasticity of cell migration: a multiscale tuning model. *J. Cell Biol.* 188:11–19.

18. Ruprecht, V., S. Wieser, …, C. P. Heisenberg. 2015. Cortical contractility triggers a stochastic switch to fast amoeboid cell motility. *Cell.* 160:673–685.

19. Renkawitz, J., and M. Sixt. 2010. Mechanisms of force generation and force transmission during interstitial leukocyte migration. *EMBO Rep.* 11:744–750.

20. Barry, N. P., and M. S. Bretscher. 2010. Dictyostelium amoebae and neutrophils can swim. *Proc. Natl. Acad. Sci. USA.* 107:11376–11380.

21. Van Haastert, P. J. 2011. Amoeboid cells use protrusions for walking, gliding and swimming. *PLoS One.* 6:e27532.

22. Howe, J. D., N. P. Barry, and M. S. Bretscher. 2013. How do amoebae swim and crawl? *PLoS One.* 8:e74382.

23. Lim, F. Y., Y. L. Koon, and K.-H. Chiam. 2013. A computational model of amoeboid cell migration. *Comput. Methods Biomech. Biomed. Engin.* 16:1085–1095.

24. Bae, A. J., and E. Bodenschatz. 2010. On the swimming of Dictyostelium amoebae. *Proc. Natl. Acad. Sci. USA.* 107:E165–E166.

25. Wang, Q., and H. G. Othmer. 2016. Computational analysis of amoeboid swimming at low Reynolds number. *J. Math. Biol.* 72:1893–1926.

26. Campbell, E. J., and P. Bagchi. 2017. A computational model of amoeboid cell swimming. *Phys. Fluids.* 29:101902.

27. Stone, H. A., and A. D. Samuel. 1996. Propulsion of microorganisms by surface distortions. *Phys. Rev. Lett.* 77:4102–4104.

28. O'Neill, P. R., J. A. Castillo-Badillo, …, N. Gautam. 2018. Membrane flow drives an adhesion-independent amoeboid cell migration mode. *Dev. Cell.* 46:9–22.e4.

29. Vargas, P., P. Maiuri, …, A. M. Lennon-Duménil. 2016. Innate control of actin nucleation determines two distinct migration behaviours in dendritic cells. *Nat. Cell Biol.* 18:43–53.

30. Valignat, M.-P., O. Theodoly, …, A. C. Lellouch. 2013. T lymphocytes orient against the direction of fluid flow during LFA-1-mediated migration. *Biophys. J.* 104:322–331.

31. Henry, S. J., J. C. Crocker, and D. A. Hammer. 2014. Ligand density elicits a phenotypic switch in human neutrophils. *Integr. Biol.* 6:348–356.

32. Gorina, R., R. Lyck, …, B. Engelhardt. 2014. β2 integrin-mediated crawling on endothelial ICAM-1 and ICAM-2 is a prerequisite for transcellular neutrophil diapedesis across the inflamed blood-brain barrier. *J. Immunol.* 192:324–337.

33. Krummel, M. F., R. S. Friedman, and J. Jacobelli. 2014. Modes and mechanisms of T cell motility: roles for confinement and Myosin-IIA. *Curr. Opin. Cell Biol.* 30:9–16.

34. Wilson, K., A. Lewalle, …, G. Charras. 2013. Mechanisms of leading edge protrusion in interstitial migration. *Nat. Commun.* 4:2896.

35. Strale, P.-O., A. Azioune, …, V. Studer. 2016. Multiprotein printing by light-induced molecular adsorption. *Adv. Mater.* 28:2024–2029.

36. Pasturel, A., P.-O. Strale, and V. Studer. 2018. A generic widefield topographical and chemical photopatterning method for hydrogels. *bioRxiv* https://doi.org/10.1101/370882.

37. Galland, R., G. Grenci, …, J. B. Sibarita. 2015. 3D high- and super-resolution imaging using single-objective SPIM. *Nat. Methods.* 12:641–644.

38. Pettersen, E. F., T. D. Goddard, …, T. E. Ferrin. 2004. UCSF Chimera–a visualization system for exploratory research and analysis. *J. Comput. Chem.* 25:1605–1612.

39. Berg, S., D. Kutra, …, A. Kreshuk. 2019. ilastik: interactive machine learning for (bio)image analysis. *Nat. Methods.* 16:1226–1232.

40. Preira, P., M.-P. Valignat, …, O. Théodoly. 2013. Single cell rheometry with a microfluidic constriction: quantitative control of friction and fluid leaks between cell and channel walls. *Biomicrofluidics.* 7:24111.

41. Theodoly, O., Z.-H. Huang, and M.-P. Valignat. 2010. New modeling of reflection interference contrast microscopy including polarization and numerical aperture effects: application to nanometric distance measurements and object profile reconstruction. *Langmuir.* 26:1940–1948.

42. Doyle, A. D., F. W. Wang, …, K. M. Yamada. 2009. One-dimensional topography underlies three-dimensional fibrillar cell migration. *J. Cell Biol.* 184:481–490.

43. Luo, X., L. Aoun, …, O. Theodoly. Different integrins mediate haptotaxis of T lymphocytes towards either lower or higher adhesion zones. *bioRxiv*, doi: 10.1101/509240.

44. Fritz-Laylin, L. K., M. Riel-Mehan, …, R. D. Mullins. 2017. Actin-based protrusions of migrating neutrophils are intrinsically lamellar and facilitate direction changes. *eLife.* 6:e26990.

45. Bernitt, E., C. G. Koh, …, H.-G. Döbereiner. 2015. Dynamics of actin waves on patterned substrates: a quantitative analysis of circular dorsal ruffles. *PLoS One.* 10:e0115857.

46. Bornens, M., M. Paintrand, and C. Celati. 1989. The cortical microfilament system of lymphoblasts displays a periodic oscillatory activity in the absence of microtubules: implications for cell polarity. *J. Cell Biol.* 109:1071–1083.

47. Paluch, E., M. Piel, …, C. Sykes. 2005. Cortical actomyosin breakage triggers shape oscillations in cells and cell fragments. *Biophys. J.* 89:724–733.

48. Lighthill, M. J. 1952. On the squirming motion of nearly spherical deformable bodies through liquids at very small Reynolds numbers. *Commun. Pure Appl. Math.* 5:109–118.

49. Maiuri, P., J. F. Rupprecht, …, R. Voituriez. 2015. Actin flows mediate a universal coupling between cell speed and cell persistence. *Cell.* 161:374–386.

50. Batchelder, E. L., G. Hollopeter, …, J. Plastino. 2011. Membrane tension regulates motility by controlling lamellipodium organization. *Proc. Natl. Acad. Sci. USA.* 108:11429–11434.

51. Brinkman, H. C. 1949. A calculation of the viscous force exerted by a flowing fluid on a dense swarm of particles. *Flow Turbul. Combus.* 1:27.

52. Somasundaram, B., J. C. Norman, and M. P. Mahaut-Smith. 1995. Primaquine, an inhibitor of vesicular transport, blocks the calcium-release-activated current in rat megakaryocytes. *Biochem. J.* 309:725–729.

53. Poincloux, R., O. Collin, …, P. Chavrier. 2011. Contractility of the cell rear drives invasion of breast tumor cells in 3D Matrigel. *Proc. Natl. Acad. Sci. USA.* 108:1943–1948.

54. Blaser, H., M. Reichman-Fried, …, E. Raz. 2006. Migration of zebrafish primordial germ cells: a role for myosin contraction and cytoplasmic flow. *Dev. Cell.* 11:613–627.

55. Shih, W., and S. Yamada. 2010. Myosin IIA dependent retrograde flow drives 3D cell migration. *Biophys. J.* 98:L29–L31.

56. Faure-André, G., P. Vargas, …, A. M. Lennon-Duménil. 2008. Regulation of dendritic cell migration by CD74, the MHC class II-associated invariant chain. *Science.* 322:1705–1710.

57. Liu, Y.-J., M. Le Berre, …, M. Piel. 2015. Confinement and low adhesion induce fast amoeboid migration of slow mesenchymal cells. *Cell.* 160:659–672.

58. Jay, P. Y., P. A. Pham, …, E. L. Elson. 1995. A mechanical function of myosin II in cell motility. *J. Cell Sci.* 108:387–393.

59. Leshansky, A. M., O. Kenneth, …, J. E. Avron. 2007. A frictionless microswimmer. *New J. Phys.* 9:145.

60. Samuelsson, M., K. Potrzebowska, …, L. Svensson. 2017. RhoB controls the Rab11-mediated recycling and surface reappearance of LFA-1 in migrating T lymphocytes. *Sci. Signal.* 10:eaai8629.

61. Paul, N. R., G. Jacquemet, and P. T. Caswell. 2015. Endocytic trafficking of integrins in cell migration. *Curr. Biol.* 25:R1092–R1105.

62. Arjonen, A., J. Alanko, …, J. Ivaska. 2012. Distinct recycling of active and inactive β1 integrins. *Traffic.* 13:610–625.

63. De Franceschi, N., H. Hamidi, …, J. Ivaska. 2015. Integrin traffic - the update. *J. Cell Sci.* 128:839–852.

64. Stanley, P., S. Tooze, and N. Hogg. 2012. A role for Rap2 in recycling the extended conformation of LFA-1 during T cell migration. *Biol. Open.* 1:1161–1168.

65. Paluch, E. K., and E. Raz. 2013. The role and regulation of blebs in cell migration. *Curr. Opin. Cell Biol.* 25:582–590.

66. Charras, G., and E. Paluch. 2008. Blebs lead the way: how to migrate without lamellipodia. *Nat. Rev. Mol. Cell Biol.* 9:730–736.

67. Paluch, E., C. Sykes, …, M. Bornens. 2006. Dynamic modes of the cortical actomyosin gel during cell locomotion and division. *Trends Cell Biol.* 16:5–10.

68. Lämmermann, T., and M. Sixt. 2009. Mechanical modes of 'amoeboid' cell migration. *Curr. Opin. Cell Biol.* 21:636–644.

69. Reversat, A.…, 2019. Adhesion-free cell migration by topography-based force transduction. *bioRxiv* https://doi.org/10.1101/793919.

70. Stroka, K. M., H. Jiang, …, K. Konstantopoulos. 2014. Water permeation drives tumor cell migration in confined microenvironments. *Cell.* 157:611–623.

71. Huerre, A., O. Theodoly, …, M. C. Jullien. 2015. Droplets in microchannels: dynamical properties of the lubrication film. *Phys. Rev. Lett.* 115:064501.

72. Strale, P.-O., A. Azioune, …, V. Studer. 2016. Multiprotein printing by light-induced molecular adsorption. *Adv. Mater.* 28:2024–2029.

Biophysical Journal, Volume *119*

Supplemental Information

Amoeboid Swimming Is Propelled by Molecular Paddling in Lymphocytes

Laurene Aoun, Alexander Farutin, Nicolas Garcia-Seyda, Paulin Nègre, Mohd Suhail Rizvi, Sham Tlili, Solene Song, Xuan Luo, Martine Biarnes-Pelicot, Rémi Galland, Jean-Baptiste Sibarita, Alphée Michelot, Claire Hivroz, Salima Rafai, Marie-Pierre Valignat, Chaouqi Misbah, and Olivier Theodoly

Movies

Movie 1 : **From Crawling to Swimming in the vicinity of a substrate.** (Left) Crawling on adhering ICAM-1-treated substrate. (Right) Swimming on Pluronic© F127 treated surface. First sequence, 20x bright field transmission microscopy, then 63x bright field transmission microscopy and finally x63 reflected interference contrast microscopy.

Movie 2 : **3D imaging of primary human effector T lymphocyte swimming in spinning disk microscopy.** Videomicroscopy sequence of swimming T lymphocytes stained with CMFDA (5-chloromethylfluorescein diacetate) on Pluronic© F127 treated surface for 14 min 40 sec with a time lapse every 20 s and stack of 10 slices taken every 1 µm. Some unpolarized cells do not swim. The arrow points a polarized and swimming cell that crosses the whole field of view. Scale bars in µm indicated on axis, magnification: 63X.

Movie 3 : **Immediate transition between crawling and swimming**. Migration on alternative 40 µm wide stripes of adherent ICAM-1 and non-adherent Pluronic© F127 prepared by LIMAP[31]. Superimposition of fluorescent image (ICAM-1, red), bright filed transmission image (greyscale) and reflection interference contrast microscopy image (bright green corresponds to cells adhesion fingerprints) taken at 63x.

Movie 4 : **Swimming in bulk suspension.** Movie of two cells suspended in a medium of matched density using a microscope tilted by 90°and a flow chamber oriented vertically for sideway observations.

Movie 5 : **Correlation of swimming direction with cell polarization axis**. T lymphocytes swimming on Pluronic© F127 treated surface imaged in bright field at 10x of primary human effector. The red bars direction represents the instant tangent to trajectory, and their norm is proportional to the ratio between instant speed and maximal speed reached by the cells. The yellow bars direction represents the orientation of the ellipse having the same second-moment as the segmented cell, and their norm scales with the value of the ellipse eccentricity, as (exp(ecc)-1)/(exp(1)-1), where ecc is the eccentricity of the ellipse which varies between 0 and 1. (For more details see Suppl. Mat. Figure S 3 and corresponding paragraph).

Movie 6 : **Role of actomyosin network in swimming motion.** Movies in bright field at 63x of primary human effector T lymphocytes swimming on Pluronic© F127 treated surface in the presence of actin inhibitors: control, 50 µM Blebbistatin, 0.05 µM Latrunculin or 100 µM CK666. Scale bar 20 µm.

Movie 7 : **3D live imaging by so-SPIM of the actin cytoskeleton of swimming primary human effector T lymphocyte**. Video microscopy movie of RFP-Lifeact transfected cell, showing lamellar-protrusion forming with random orientation in cell front and travelling backwards at around 10 $\mu m.min^{-1}$.

Movie 8 : **Live bright field imaging of swimming primary human effector T lymphocytes showing protrusion retrograde motion and nucleus forward squeezing through constricted rings**. Bright field videomicroscopy at 63x of primary human effector T lymphocytes swimming on Pluronic© F127 treated surface. Scale bars 10 µm.

Movie 9 : **Swimming of a cell by the motion of two blebs on the cell surface.** The color here represents the mean curvature of the cell surface.

Movie 10 : **Lymphocytes swimming with perturbation of cell body deformation**. Bright field videomicroscopy at 63x of primary human effector T lymphocytes swimming on Pluronic© F127 treated surface in pure medium (left) and in a medium diluted with water at 50% (right). Osmotic

stress cancels the deformations of cell body by swelling but cell speed is 8 μm.min^{-1} like for control cells.

Movie 11 : **Cell membrane retrograde flow revealed by attached beads**. Bright field videomicroscopy of ICAM-coated beads travelling from front to back on the cell membrane of swimming T-cells in HBSS control media, 50 μM Blebbistatin, 0.05 μM Latrunculin, or 100 μM CK666.

Movie 12 : **Numerical simulation of swimming by retrograde flow.** Cell shape is extracted from experiments. The swimming is shown in the laboratory frame. Color code on the surface represents the production/consumption of the cortex material. Small spheres are fictitious tracers moving with the cortex velocity. Transmission coefficient θ = 1.

Movie 13 **: Evidence that actin bound proteins LFA-1 are advected backwards at cell membrane whereas non actin bound proteins MHC-1 are diffusive**. TIRF-FRAP experiments on primary human effector T-cell (Top left) transfected with a GFP-Actin by lentiviral infection, (Top right) stained with membrane lipidic marker DiO, (Bottom left) stained with antibody Mab24 that binds an actin-bound protein, the integrin LFA-1 in its high affinity state, and (Bottom right) stained with anti-HLA-ABC that binds the non-actin-bound MHC-1 type I proteins. Scale bars 5 μm.

Movie 14 : **Cytoskeleton retrograde flow**. TIRF imaging of a primary human effector T lymphocyte transfected with GFP-Actin and displaying backward travelling of clusters. Scale bar 5 μm.

Movie 15 : **Single cell evidence of average backward advection for actin-bound LFA-1 and average absence of motion for non-actin-bound MHC-1.** TIRF images after FRAP bleaching of a line pattern revealing actin-bound activated LFA-1 in its high affinity state (left) and non-actin-bound MHC-1 (right). Scale bar 5 μm.

Movie 16 : **Evidence that advected proteins LFA-1 are recycled at the cell front by internal vesicular transport whereas diffusive proteins MHC-1 are not**. TIRF-FRAP experiments on primary human effector T-cell (Right) stained with antibody Mab24 that binds the actin-bound proteins LFA-1 in high affinity state, and (Left) stained with anti-HLA-ABC that binds the non-actin-bound proteins MHC-1. The cell front is frapped and fluorescence recovers only from the front for LFA-1, in agreement with an internal vesicular recycling of integrins from back to front, and only from the rear for HLA, in accord with a surface diffusion mechanism.

Movie 17 : **Lymphocytes are motile when confined between non-adherent plates.** Movies in bright field at 20x of primary human effector T lymphocytes moving between two glass substrates patterned with an adherent zone covered with ICAM-1 (left) and an anti-adhesive zone (right). The round shapes correspond to 100 μm diameter glass pillars that sustain the structure.

Movie 18 : **Lymphocytes are motile when confined in tubes.** Movies in bright field at 63x of a primary human effector T lymphocytes moving in a non-adherent microfluidic channel of cross-section 4 x 4 μm^2.

Supplementary information on swimming speed experiments

Cells are non-adherent on Pluronics-treated substrates

Interference contrast microsocopy was used to assess the adhesion states of lymphocytes on 2D substrates. In Figure S 1 RICM images were inverted, thresholded and colored in green. The green zones correspond therefore to the adherent contact zone of cells. The projected area of cells was determined from the contour of the cells imaged in bright field. Cell adhesion was then quantified for each cell by the ratio of adherent area versus the projected area. Most polarized cells were adherent on ICAM-1 substrates with a mean adhesion in projected area of 40 ± 15 %. In contrast, 100 % of polarized cells had an adhesion in projected area lower than 5 % on Pluronics substrates, which corresponded to background level and therefore no detectable adhesion.

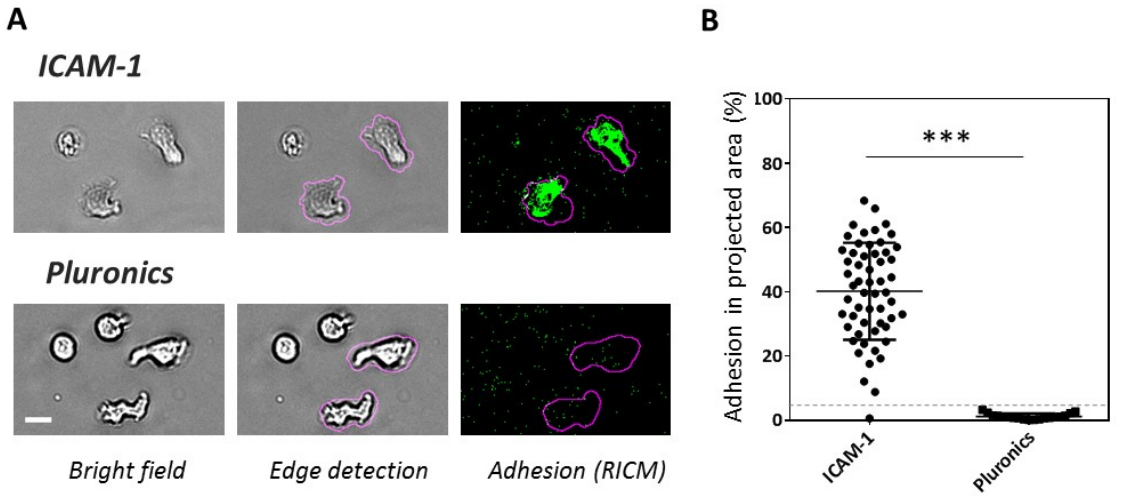

Figure S 1 : **RICM quantification of cell adherence on substrates coated with ICAM-1 and Pluronics: (A)** Microscopy data on ICAM-1 (top) and Pluronics (bottom) treated substrates. **Left-** Bright field images. **Middle-** Cell outlines determined using ilastik. **Right-** Superposition of cell contours with inverted (white signal on dark background) RICM images, application of rolling ball algorithm (to flatten the image with 10pix kernel size), and thresholding above background levels (with same threshold for all images). **(B)** Quantification of the adhesion area (determined by RICM signal) in the projected area of each cell (determined by the cell contours). Each point corresponds to one cell. Nexperiments = 3, Ncells = 57 for ICAM-1, Ncells = 21 for Pluronics, ***P < 0.001 (two-tailed Student's t test).

Experimental swimming speeds in suspension are independent of distance to a wall

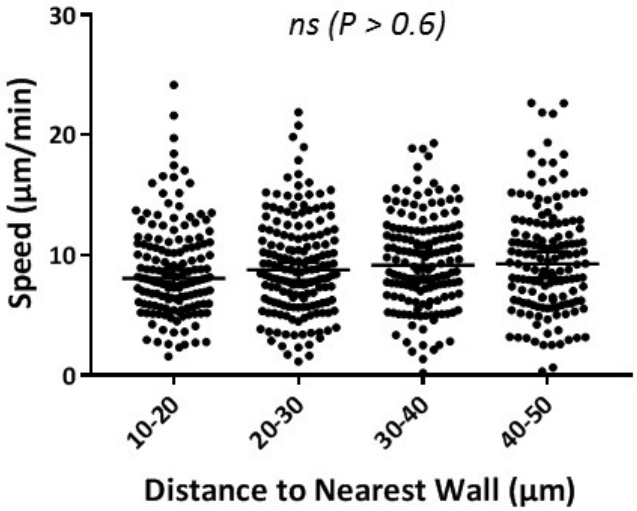

Figure S 2 : Swimming speed of active cells in suspension measured using the set-up of Figure 3 as a function of the distance to the nearest wall. Each data point corresponds to one step motion of a swimming cell for an interval of 30 s. Nexperiments = 10, Ncells = 66 Nsteps > 620. *P < 0.05, **P < 0.001, ***P < 0.001, with respect to distance to nearest wall, one way ANOVA with post Turkey's multiple test.

Propulsion of non-adherent cells is directed along polarization axis and toward lamellipod

The angular difference between the direction of polarization of cells migrating on an non adherent substrate and their instant displacement direction was determined on bright field images at magnification x20 (Movie 5). Binary images were analyzed in Matlab using the built-in *regionprops* function providing the orientation of the ellipse having the same second-moment as the segmented cell, and its eccentricity defined as the ratio between the foci of the ellipse and its major axis length. The direction of instant displacement was calculated on 30s time intervals. The angle calculated between cell orientation and direction of instant displacement was defined as the acute angle between both lines, taken positively. Thus this angle reached minimal value 0° when both directions are parallel or anti-parallel, and maximal value 90° when they are orthogonal. In order to select active cells, the histograms took into account all instant configurations of cell shape orientation and displacement direction provided that they reach a certain level of polarization and motility (eccentricity>0.5, instant speed>5um/mn). In order to have a negative control without correlations between cell shape and cell motion direction, we analyzed image sequences of fixed cells and released the constraints on polarization and motility levels. For active cells, either in normal medium or with blebbistatin treatment, histograms of Figure S 3 show a maximum probability for cell motion

collinear to cell polarization, whereas for fixed cells there is no preferential orientation of motion (The spikes at selected angles such as 45°are artefacts due to pixellisation that favor angle calculated with finite number of pixels). Altogether, this analysis shows cell activity and cell polarization are linked to the process of non-adherent migration and swimming, and that cells always progress in the direction of their lamellipod. Interestingly, cells treated with blebbistatin display a stronger correlation between motion directivity and polarization axis (SD equals 19.7 for blebbistatin versus 27.1 for control). This suggests that the contractility and the subsequent strong shape deformations of control cells are a source of stochasticity that hinders directionality.

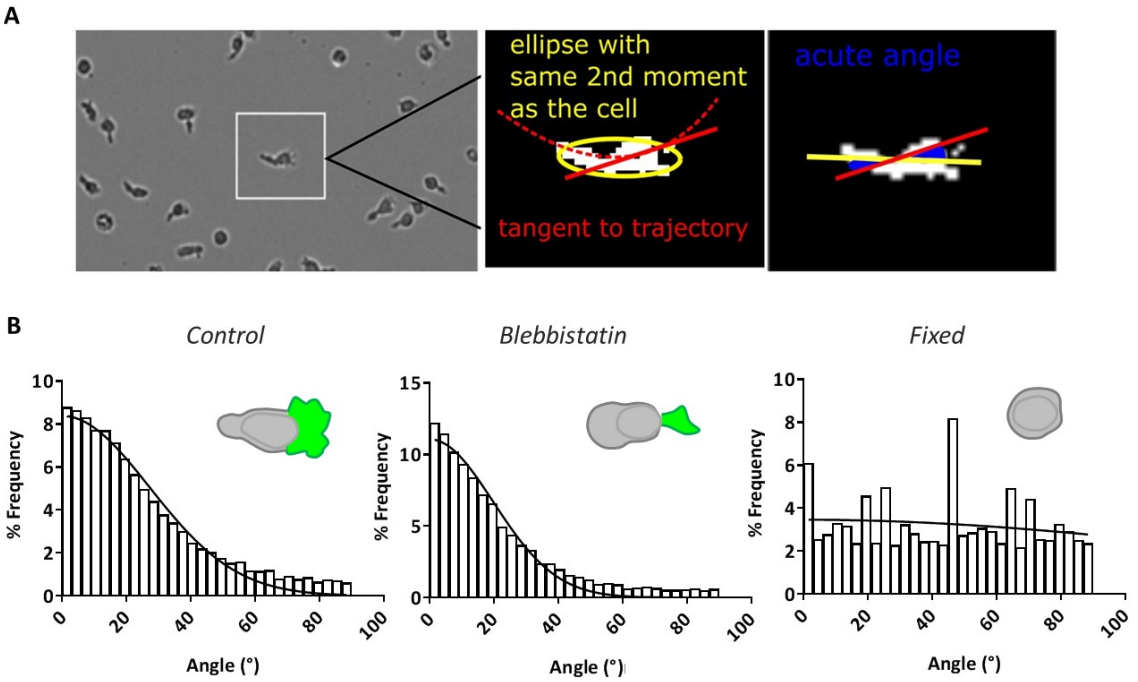

Figure S 3 : **Propulsion of non-adherent cells correlates with polarization. (A)** *Rationale of the analysis to extract direction of polarization and of instant displacement for individual cells.* ***Left-*** *Image source taken at magnification x10.* ***Middle-*** *Direction of instant displacement (red) is the tangent of the cell trajectory (between 3 points taken every 30 s), and direction of polarization (yellow) is the main axis of the ellipse corresponding to the second moment of cell contour.* ***Right-*** *The angle between direction of polarization and displacement is taken as the acute angle between their axis of orientation. (***B)** *Frequency of motion events versus the angle between cell polarization and direction of instant displacement for active cells in normal medium (**left**), active cells treated by Nlebbistatin (**middle**), and fixed cells (**right**). The drawings are schematics of cells morphology with cell body (grey) and lamellipod (green). The solid lines correspond to fits by a single Gaussian centered*

to a mean of zero. The standard deviation of the Gaussian is SD = 27.1° for control cells, SD = 19.7° for Blebbistatin treated cells and SD = 131.1° for fixed cells. Ncell = 226, 860, 92 and Nevents = 12411, 13646 and 12531 for respectively control, Blebbistatin and fixed cells. The histograms are normalized with respect to the total number of events. (See also Movie 5)

Experimental swimming speeds are independent of medium viscosity increase up to 100 times

Hydrodynamic interactions between an amoeboid lymphocyte and a fluid are sufficient to promote momentum transfer. In order to test how the viscosity of the medium influences the efficiency of cell-fluid coupling, we performed swimming experiments in culture medium supplemented with dextran of molecular weight 2,000 kDa to increase its viscosity to 10 and 100 times. Viscosity of solutions were measured on a Bohlin Gemini 150 rheometer equipped with cone-plate geometry (cone angle 20° , diameter 60 mm) at T=22°C (Figure S 4 –A). A control of the effect of osmotic pressure was performed with dextrose solution. Figure S 4 –B displays the histogram of cells speeds versus viscosities and osmotic pressure. The data in control medium and medium with dextrose are fitted with a double Gaussian, the Gaussian with lower mean speed corresponding to inactive and diffusing cells, the Gaussian with higher mean speed corresponding to active and swimming cells. The data in medium of increased viscosities were fitted by a single Gaussian because the inactive cells had a very low apparent mean speed and were sorted out by our tracking protocol. Figure S 4-C shows that apparent mean speed of inert and diffusing objects are indeed below 0.5 μm/min. The statistical analysis of speed for active cells (Figure S 4-D) shows that osmotic pressure had no significant effect on swimming speed within the range tested for viscosity measurements. For a viscosity increase by 10x, we observed a decrease of speed by 25 % that was statistically significant. However, this tendency of speed decrease with viscosity was not confirmed by a further increase of viscosity by 100x, for which the speed is found statistically similar as for the control. These observations support therefore the idea that viscosity plays no determinant role in propulsion speed, which is consistent with predictions of the model for swimming propelled by cell membrane retrograde flow or by protrusions.

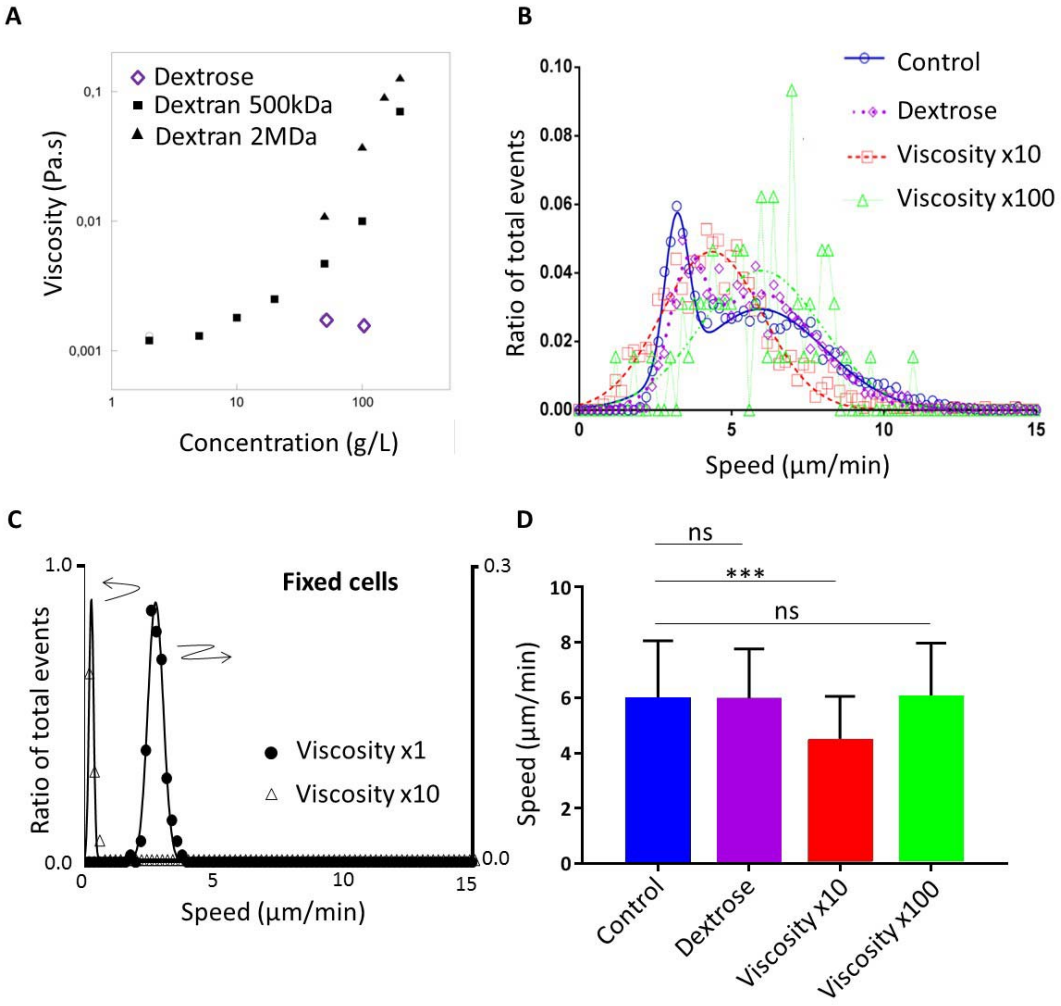

Figure S 4 : **Cell speed is independent of the medium viscosity. (A)** Viscosity of Dextran and dextrose solutions in HBSS versus concentration. **(B)** Histogram of raw curvilinear speed for cells in normal medium and medium with viscosity increased 10 x (Dextran 2,000 kDa at 50g/L) and 100 x (Dextran 2,000 kDa at 150g/L), and osmotic control condition (Dextrose 16g/L). Lines correspond to fit by a double Gaussian for normal medium and Dextrose and by a single Gaussian for medium of increased viscosity (10x and 100x). **(C)** Histogram of raw curvilinear speed for fixed cells in normal medium (filled dots) and in medium of viscosity x10, Dextran 2,000 kDa at 50g/L (Hollow triangles). **(D)** Average speed and standard deviation of active cells determined by the Gaussian fit of higher mean speed for normal medium and dextrose and by the single Gaussian for medium of increased viscosity. Ncells = 4342 (HBSS), 1262 (Dextran 50 $g.L^{-1}$), 64 (Dextran 150 $g.L^{-1}$), 1449 (Dextrose),), 139 (Fixed viscosity x1), 30 (Fixed viscosity x10); Nexperiments = 5 (HBSS), 3 (Dextran 50 $g.L^{-1}$), 3 (Dextran 150 $g.L^{-1}$), 2 (Dextrose), 2 (Fixed viscosity 1x), 2 (Fixed viscosity 10x). *P < 0.05, **P < 0.001, ***P < 0.001 with respect to control, one way ANOVA with post Turkey's multiple test.

Supplementary Table

Table 1 : Swimming speed versus the effects of cell fixation, medium viscosity change and actin inhibitors addition. The table reports the raw swimming speed estimated by averaging the instant curvilinear speeds between two positions of cell mass centre separated by 30s for each cell. Average raw speeds of active and passive cells as well as fraction of active cells extracted from the fit of the speeds histograms by a double Gaussian (Figure 2**Error! Reference source not found.**-B). Speed errors correspond to standard deviation. Cell number correspond to the number of cells considered for each experimental condition.

	Active cells		**Passive cells**	
Condition	**($\mu m.min^{-1}$)**	**Fraction**	**($\mu m.min^{-1}$)**	**Number of cells**
HBSS-CTRL	5.9 ± 2.1	78%	3.2 ± 0.4	4342
Blebbistatin	4.3 ± 1.1	45%	3.1 ± 0.4	2353
CK666	4.4 ± 0.8	21%	3.2 ± 0.4	5582
Latrunculin	4.2 ± 0.5	20%	3.3 ± 0.4	2255
Bleb. + Lat.	5.0 ± 0.3	2%	3.4 ± 0.3	403
HBSS-PFA	-	-	2.8 ± 0.3	139
Viscosity 10x	4.4 ± 1.6	NA	-	1262
Viscosity 100x	6.0 ± 2	NA	-	64
Dextrose	5.9 ± 1.8	80%	3.6 ± 0.6	1449
Visco 10x-PFA	-	-	0.27 ± 0.09	30
ICAM-1	14.6 ± 7.5	-	-	503

Supplemental information on swimming mechanism

Cell diffusion and persistent swimming: Model

We model the motion of the cells as a combination of deterministic swimming and random noise. The swimming velocity $v_s = v_s p$ is assumed to have a constant absolute value but the orientation vector p can vary in time. The random noise here consists of translational diffusion with diffusion coefficient D_t and rotational diffusion with angular diffusion coefficient D_r. This noise accounts both for thermal fluctuations and for the active dynamics of the cell. Since cells are swimming close to a wall, the dynamics of orientation p and position r of the swimmer are effectively two-dimensional. The model described above belongs to a broad class of persistent random walk problems, which have enjoyed a lot of attention in the literature[1] . We therefore give here only a brief overview of the solution process and the final expression of the mean square displacement of the cell as a function of time and the model parameters.

Cell diffusion and persistent swimming: Solution

We first calculate the correlation $\langle p(t_0) \cdot p(t) \rangle$. The probability density function $\psi(p,t)$ for the swimmer to have orientation p at time t satisfies the following equation:

Equation 1 $$\dot{\psi}(p,t) = D_r \nabla_p^2 \psi(p,t).$$

where $\nabla_p \equiv (I - p \otimes p) \cdot \partial_p$ is the gradient operator on a unit circle representing possible orientations of p, and I is the identity matrix. The right hand side of Equation 1 expresses the angular diffusion process. If $p(t_0) = p_0$, the initial condition for Equation 1 is

Equation 2 $$\psi(p,t_0) = \delta_p(p - p_0),$$

where δ_p is the Dirac function. Equation 1 is solved by expanding $\psi(p,t)$ in Fourier harmonics of p, which represents the eigenfunctions of the Laplace operator ∇_p^2:

Equation 3 $$\psi(p,t) = 1 + \psi_i(t) p_i + \psi_{ij}(t) p_i p_j + \ldots,$$

where $\psi_{ij}(t)$ and so on are symmetric and traceless. The quantity of interest here is $\psi_i(t) = 2\langle p_i(t) \rangle$. Substituting Equation 3 into Equation 1 yields $\psi_i(t) = \psi_i(t_0) exp[D_r(t_0 - t)]$ for $t \geq t_0$, resulting in

Equation 4 $$\langle p(t_0) \cdot p(t) \rangle = p(t_0) \cdot \langle p(t) \rangle = e^{-D_r|t-t_0|}.$$

The displacement due to persistent motion is calculated by integrating Equation 4:

Equation 5

$$\partial_t \langle [r(t) - r(t_0)]^2 \rangle = 2\langle v_s(t) \cdot [r(t) - r(t_0)] \rangle = 2 \int dt' \langle v_s(t) \cdot v_s(t') \rangle = 2v_s^2 \frac{1 - e^{-D_r|t-t_0|}}{D_r}.$$

Integrating Equation 5 and adding the contribution of the translational diffusion yields

Equation 6 $$\langle [r(t) - r(t_0)]^2 \rangle = \frac{2v_s^2}{D_r} \left(|t - t_0| + \frac{e^{-D_r|t-t_0|} - 1}{D_r} \right) + 4D_t|t - t_0|.$$

Equation 6 reduces to Equation 1 for $tD_r \ll 1$.

Model of swimming by blebs

In order to simulate the bleb-driven swimming of the cells, we model the cell as an elastic capsule, to which active forces are applied, while maintaining the zero net force and torque conditions (Figure S 5). The application of the active force density concentrated in small regions of the cell surface results in the formation of bleb-like protrusions. Further, the location at which the active forces are applied is moved with a prescribed velocity v_{bleb} along the surface of the cell. In addition to the magnitude of the active force and the bleb velocity, the life-time of the blebs, T_{bleb}, is also an important parameter that describes the duration for which the active force is applied. This application of time dependent active force leads to formation and movement of the blebs along the cell surface. The shape and size of the blebs depends on the material properties of the cell, small bending stiffness, leading to larger and more protrusive blebs.

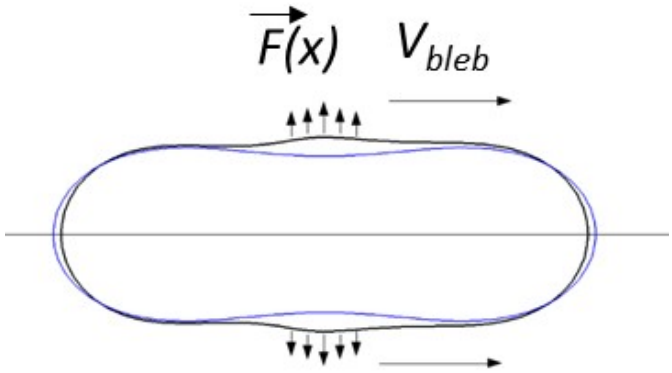

Figure S 5 : Schematic of a swimming cell by protrusive blebs. Blue and black contours are the initial and deformed configurations of the cell, respectively.

The configuration of the cell during the course of a bleb formation and motion is shown in Figure S 6 , and the maximum size of the blebs for different values of active force amplitudes is shown in Figure S 7.

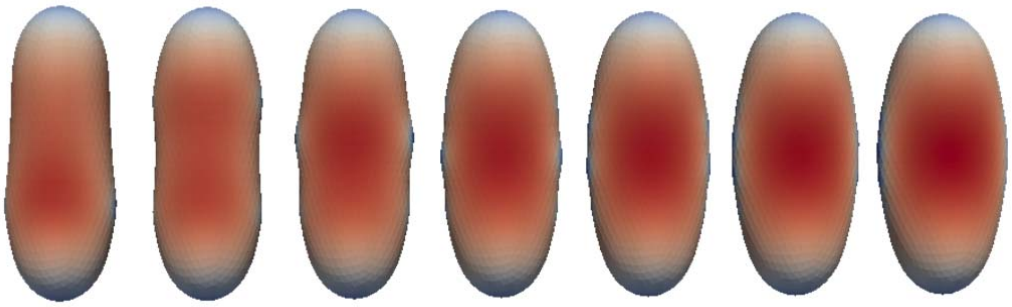

Figure S 6 : Configuration of the cells with a single pair of blebs at different time points. Progression of time is from left to right.

The swimming velocity is then obtained by solving the hydrodynamic problem in fluids inside and outside the cell, as described below and the velocity of the cell by the motion of a single pair of blebs is shown in Figure S 7-B. For all the simulations $v_{bleb}$was fixed at 0.02 and force amplitude *F* was varied. The plot shows that in bleb-driven swimming, the cell velocity $v_{cell} < 10^{-3} v_{bleb}$. Furthermore, the dependence of the swimming velocity on the force amplitude is $v \propto F^2$.

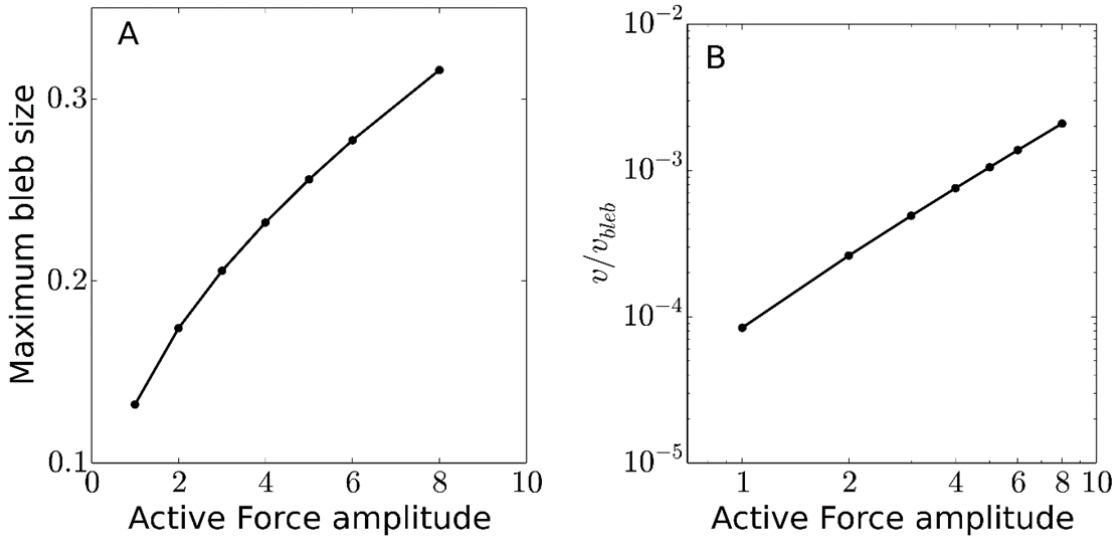

Figure S 7 : **(A)** Maximum size of the blebs for different values of active force amplitudes (see Figure S 5). **(B)** Dependence of average cell velocity $v_{cell} < 10^{-3} v_{bleb}$ on the active force amplitude. Here the bleb velocity relative to the cell centre has been kept fixed at $v_{bleb} = 0.02$.

Quantification by wavelet transform of experimental protrusion propagation modes

We tracked the cell contours of migrating cells image at magnification x60 in three conditions: (i) the "control condition", in normal medium, (ii) the " water condition" in a medium including 50% of

water, and (iii) the "blebbistatin condition", in a medium with a concentration of 50µM of Blebbistatin.

From the cell contour to cell edge to cell center distance kymographs

The cell contours were detected with the Ilastik software and the contour points exported in Matlab for further analysis. To reconstruct the contours with an homogeneous sampling around the cell perimeter, we used elliptic Fourier analysis with the "plot_fourier_approx.m" matlab function[2] to obtain a smooth contour of the cells. We used 50 modes for the reconstruction and N = 2000 points of sampling along the contour (Figure S 8-A). We then resampled a number of N = 500 points along the contour spaced by an equal curvilinear distance ds = cell perimeter/N. We calculated the distance R to each of these points to the cell barycenter (defined as the average position of all the points inside the cell contour) (Figure S 8-B). As cells from different conditions can have different average radii (the Blebbistatin condition cells are significantly smaller than the control cells), we computed the kymographs of the relative radius defined as $R \Big/ < R >_{time}^{space}$ with $< R >_{time}^{space}$ the cell average radius averaged in time and around the cell contour. The kymograph of the relative radius (with the position along the contour in the y axis and the time in the x axis) showed discontinuities that reflected potential rotations of the cell (Figure S 8-C,left). We removed these discontinuities by calculating the best shift maximizing the correlation coefficient between two consecutive kymograph columns and iteratively permuted the columns by a circular shift corresponding to the shift maximizing correlation between neighboring columns (this is equivalent to aligning consecutive images of the cell to remove its rotations). After aligning the kymograph, we shifted it circularly in order to have the lamelippodia at its center and the uropod at its two extremities (Figure S 8-C, right).

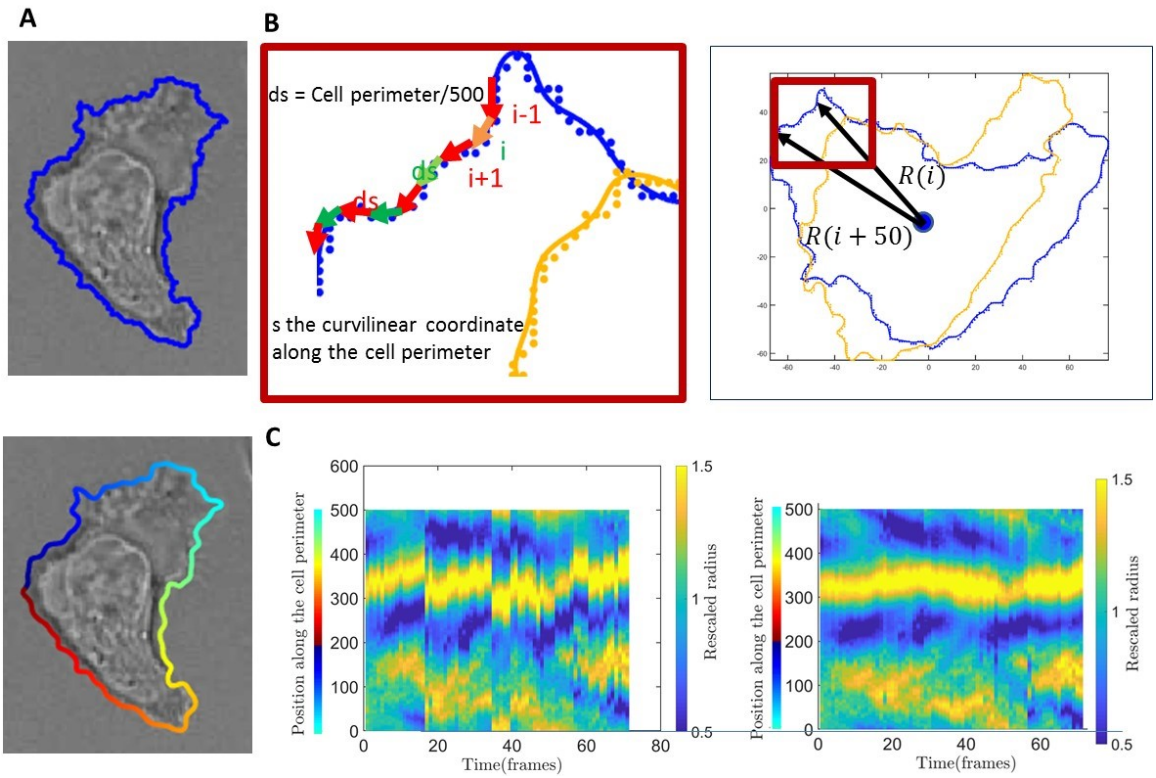

Figure S 8: Contour fluctuation analysis with Elliptic Fourier analysis. **(A) Top-** Raw cell contour extracting using Ilastik. **Bottom-** Contour from elliptic Fourier reconstruction. **(B)** Analysis of the cell edge-cell center distance, R, variations along the cell perimeter. Homogeneous sampling of step ds along the curve. **(C)** Kymographs of rescaled cell edge-cell distance before (left) and after (right) rotation correction.

Comparing the relative amplitude of cell contours waves in different conditions with wavelet spectral analysis

To analyze the waves of deformation observed qualitatively on the cells timelapses, we separated the relative radius kymograph in two parts: (i) its constant profile around the contour averaged in time, defined as the time average of the relative radius $< R >_{time} / < R >_{time}^{space}$ (it corresponds to the stable modulations of cell shape due to the polarized cell geometry during migration, with a main protrusion at the front (lamellipodia) and another one at the back (uropod)) (ii) its time varying part defined as $(R - < R >_{time}) / < R >_{time}^{space}$, which corresponds to the contour time fluctuations depending on space. We identified waves patterns in the corresponding kymograph, which can be mapped to the waves of deformation observed on the cell contours. To quantify these waves velocities and amplitude and to compare them between different cells and conditions, we then performed a 2D wavelet analysis of the kymographs using the 2D Morlet wavelet transform with the

matlab cwtft2.m function (Figure S 9). As all kymographs did not have the same temporal extension (total time between 70s and 160s) and temporal sampling (every 2 or 5s), we linearly interpolated all the kymographs at a sampling rate of 1 frame/s and we cropped big kymographs in two small kymographs of 70s in order to avoid any artefact in the wavelet analysis due to differences in kymographs size and sampling frequencies. As we analyzed the wave patterns in two dimensions, in order that the waves appear with reasonable angles in 2D, we subsampled by linear interpolation the kymograph in the y axis (the contour position axis), and we performed the wavelet analysis with kymographs of a fixed size of N = 68 points in the space dimension and N = 70 points in the time dimension. To obtain the wavelet spectrogram of each kymograph, we represent the magnitudes of the 2-D CWT coefficients (using the L1 norm convention) for angles between 0 and 180 degrees and scales between 8 and 60 (the scales correspond here to the periods observed in the 2D kymographs and the angles to their orientation, as any periodic pattern in the kymograph can be described by its period and its angle.) Although different cells in each condition displayed some variability, striking features appeared both on the kymographs and on the wavelet spectrograms. In the control condition, waves appeared on the spectrogram with angles close to 60 and 120 degrees and scales close to a value of 35, which corresponds to deformation waves propagating from the lamellipodia to the uropod at an average speed around a half cell perimeter/30s, or 10-20 µm/min (Figure 5-D). These waves can be identified strongly in the control and water condition. They can sometimes be identified in the blebbistatin condition but in an attenuated version and in many cases not. To quantify this feature, we computed the ensemble averaged spectrograms between all individual spectrograms in a same condition, to compare the average spectrogram for each condition Figure 5-E). We find a much lower amplitude in the blebbistatin case than in the control and water for all modes. On the main mode identified above as the waves of deformation mode, we observed a factor of 2 on the coefficients amplitude between the control and the blebbistatin, which is proportional to the average kymograph amplitude signal.

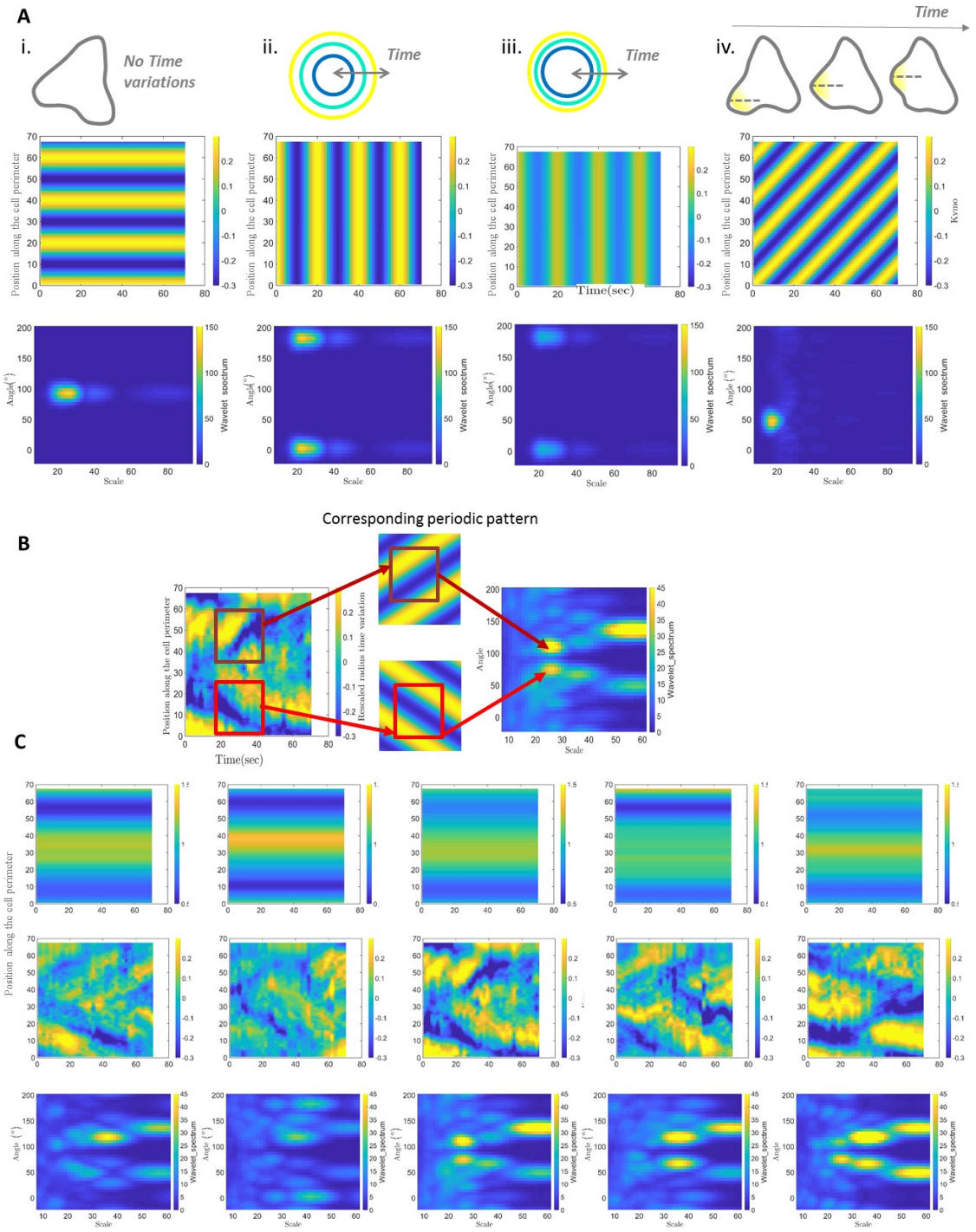

Figure S 9: Analysis with wavelets of the kymographs of cells contours. **(A)** Kymograph and wavelet spectra corresponding to ideal cases of i- a cell with irregular shape without time variations; ii and iii. a circular cell with periodic time variations of size. Amplitude in wavelet spectra reflects amplitudes of deformations; iv. cell with protrusions propagating backwards on the starboard side. **(B)** Identification in a kymograph of a cell contours (left) of the periodic patterns (middle) corresponding to a mode in the wavelet spectrum (right) of the kymograph. **(C)** Examples of time-averaged kymographs (top), corresponding kymograph with time-average contribution subtracted (middle), and corresponding wavelet spectrum (Bottom) for control cells.

Extension of the model of swimming by blebs to **multiple blebs with various size and coherence**

We have investigated further the evolution of the swimming speed in the presence of multiple protrusions (Figure S 10). We considered as an extreme limit the idealized situation where blebs move very coherently such that they form rings traveling along the surface from one pole to the other.

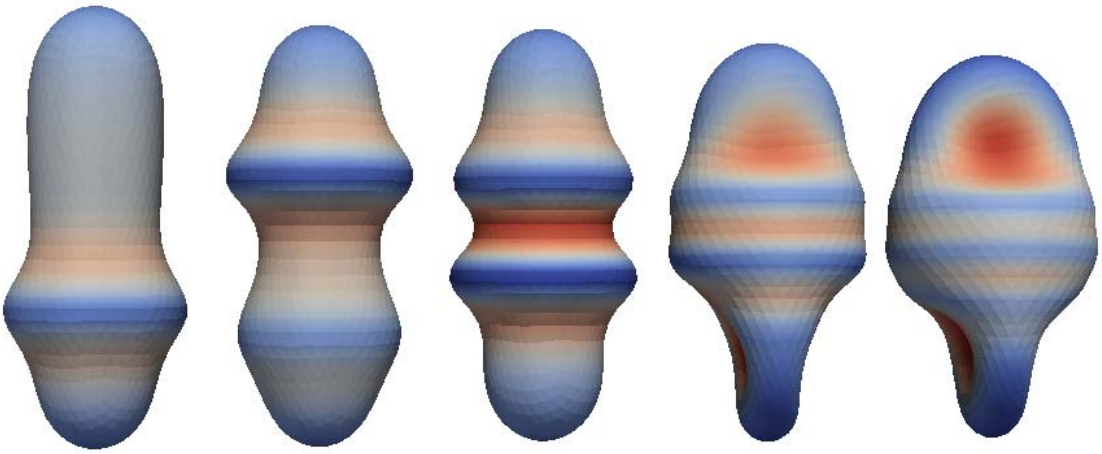

Figure S 10 : Cell shape at an instant for different number of blebs. The left most cell has only one pair of bleb at any time, the second cell has two pairs, and so on. The surface colour demonstrates the mean curvature.

The increase of their number leads to an increase of swimming speed until a value slightly less than 0.1 the retrograde flow and then drops as their number increase (Figure S 11). Note that blebs in the form of rings were never observed, meaning that locomotion caused by small waves traveling along the surface is unlikely, since the implied swimming speed would be even smaller.

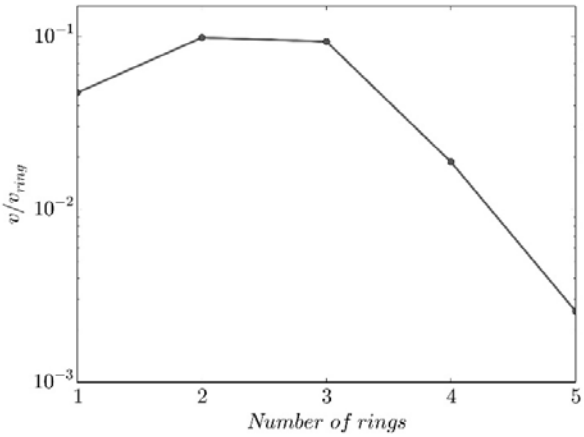

Figure S 11 : Normalized cell speed versus number of rings.

Model of swimming by membrane retrograde flow: Actin cortex flow

Actin polymerization expands the cortex in the front region of the cell, whereas myosin-induced contractility and actin depolymerization consume the cortex in the rear region of the cell. Between these regions, the actin moves from front to back along the cell membrane. An overpressure of the cortex at cell front due to actin accumulation and an underpressure at cell rear due to myosin-induced contraction can both contribute to forces driving the retrograde flow of the cortex. We thus model the driving force as the pressure gradient along the cell surface, $\nabla^S P$, where *P* is the pressure field and ∇^S is the surface gradient operator. This gradient implies a net cortex flow field $v_a(r)$ which, in a simple approximation, can be taken locally proportional to the driving force:

Equation 7 $$v_a(r) = -\mu\nabla^S P(r)$$

Where μ is a mobility coefficient. Here we assume that the shape is fixed so that the flow is tangential to the surface in the reference frame commoving with the cell. By choosing an appropriate pressure field, Equation 7 can be proven to be exact for any axisymmetric flow (see below). It is interesting to note that Equation 7 is identical to the Darcy law, valid in a porous medium or a Hele-Shaw flow. The cortex region could be viewed as a thin layer, a curved Hele-Shaw geometry, hence Equation 7 can be inferred from classical hydrodynamics. Equation 7 is closed by the mass conservation equation:

Equation 8 $$\nabla^S . v_a(r) = \psi_p(r) - \psi_d(r)$$

Here we express the change of the local 2D concentration of actin (per cortex area) due to the advection by the flow (the left hand side) through the local rate polymerization $\psi_p(r)$ (source) and the local rate of depolymerization $\psi_d(r)$ (sink). $\psi_p(r)$ and $\psi_d(r)$ are zero everywhere except in a small domain localized in the front and rear regions of the cell, respectively. Substituting Equation 7 into Equation 8 gives an equation for *P* which can be solved. Once *P* is determined the actin flow field $v_a(r)$ can be obtained from Equation 7.

Model of swimming by membrane retrograde flow: actin flow in ***an axisymmetric case***

The purpose is to show that for axisymmetric cells Equation 7 holds automatically. The cell shape and the actin velocity can be parametrized in cylindrical coordinates as

Equation 9 $$r(s,\varphi) = \big(\rho(s)cos(\varphi), \rho(s)sin(\varphi), z(s)\big),$$

Equation 10 $$v_a(s,\varphi) = v_a(s)\partial_s r(s,\varphi)$$

where s is the arclength measured from the front pole of the cell, φ is the polar angle, $\rho(s)$ and $z(s)$ are shape functions, and $\partial_s r(s,\varphi)$ is the tangent vector along the meridian. The properties of s are such that $|\partial_s r(s,\varphi)| = 1$. Equation 7 can be easily verified if we define $P(s,\varphi)$ as

Equation 11 $$P(s,\varphi) = -\frac{1}{\mu}\int v_a\,(s')ds'$$

Model of swimming by membrane retrograde flow: ***Exact solution for a spherical swimmer***

The actin flow can be obtained explicitly for a spherical cell having a point source of actin $\psi_p(r) = 2Rv_0\delta(r - r_N)$ at the North Pole r_N and a point sink $\psi_d(r) = 2Rv_0\delta(r - r_s)$ at the South Pole r_S. Here *R* is the sphere radius and v_0 is a constant having a dimension of velocity that turns out to be equal to the retrograde flow velocity at the equator in the cell frame. We present the solution in spherical coordinates. Defining the origin as the centre of the swimmer and the polar direction as source point of actin, we write the velocity at a point $(Rsin\theta cos\varphi, Rsin\theta sin\varphi, Rcos\theta)$ as

Equation 12 $$v(\theta,\varphi) = \Big(v_0\frac{cos\theta}{sin\theta}cos\varphi, v_0\frac{cos\theta}{sin\theta}sin\varphi, -v_0\Big),$$

where θ is the azimuth angle. The corresponding actin pressure is written as

Equation 13 $$P(\theta,\varphi) = \frac{v_0}{2\mu}ln\frac{1+cos\theta}{1-cos\theta}$$

The swimming velocity is then given by $v_s = \beta v_0$.

Flow outside the cell

Since the Reynolds number in the problem is extremely low, the flow v_f in the fluid outside the cell membrane satisfies the Stokes equations:

Equation 14 $$\eta_0\nabla^2 v_f - \nabla p = 0, \qquad \nabla\cdot v_f = 0,$$

where η_0 is the viscosity of the suspending medium. Equation 14 are solved together with the boundary conditions given by $v_f = 0$ at infinity and Equation 17 of the main text. The unknowns v_s and ω_s are solved for from conditions:

Equation 15 $$\int F\,dA = 0,$$

Equation 16 $$\int F \times r dA = 0,$$

where F is the surface force density applied locally by the fluid to the cell, dA is the area element and integrals are taken over the boundary of the cell membrane. Equation 15 and Equation 16 express that no external forces or torques act on the swimmer. The forces F can be expressed through the viscous stress tensor σ of the fluids

Equation 17 $$F_i = -\sigma_{ij} n_j, \quad \sigma_{ij} = \eta_0 \left(\partial_i v_{fj} + \partial_j v_{fi}\right) - p\delta_{ij},$$

where n is the outward normal to the boundary of the cell. It follows from the linearity of Equation 14 and Equation 2 of the main text that for any a, if v_f, v_s, ω_s, σ, F, and p represent a solution of the problem for a given cell shape, v_a and external fluid viscosity η_0, then v_f, v_s, ω_s, $a\sigma$, aF, and ap represent a solution of the problem for the same shape, v_a and external fluid viscosity $a\eta_0$. This implies that changing viscosity of the suspending medium does not affect the swimming velocity for the same velocity of the retrograde flow and the same transmission coefficient β. This result is consistent with experimental observations (cf. Suppl. Mat., Figure S 4 and "Experimental swimming speed are independent of medium viscosity increase up to 100 times").

Model of swimming by membrane retrograde flow: *Numerical method for any swimmer*

We parametrized the surface of the cell obtained in experiments by a triangular mesh. The Laplace equation for *P* (Equation 7 substituted in Equation 8) was solved by finding a stationary solution of a diffusion equation. The flow in the suspending fluid was solved for using the boundary integral formulation. The details of the numerical procedure and the validation are given in [3].

Vicinity of a wall is negligible

We have also solved the numerical problem for a swimmer near a solid wall. The no-slip boundary condition at the wall was imposed by taking a modified Green's function in the boundary integral formulation, as discussed in Pozrikidis C (1992)[4]. The same shape and retrograde flow field were taken as in the unconfined case. The orientation of the wall was chosen consistently with the experiment but the position was varied in order to scan different gaps between the cell and the wall. The resulting dependence of the swimming velocity (assuming $\beta = 1$) is shown in Supplemental Figure S9.

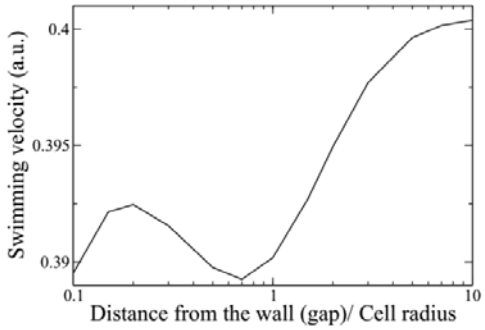

Figure S 12 : Calculated swimming velocity of cell powered by cell membrane treadmilling versus the distance of the cell to the wall normalised by the cell size. The presence of the wall influences only marginally cell speed between 0.39 and 0.4.

Quantification of LFA-1 and VLA-4 expression on effector T lymphocytes.

Quantification LFA-1 and VLA-4 number per cell was performed by quantitative cytometry (Figure S 13) and yielded an average number per cell of 25000 for LFA-1 and 15,000 for VLA-4.

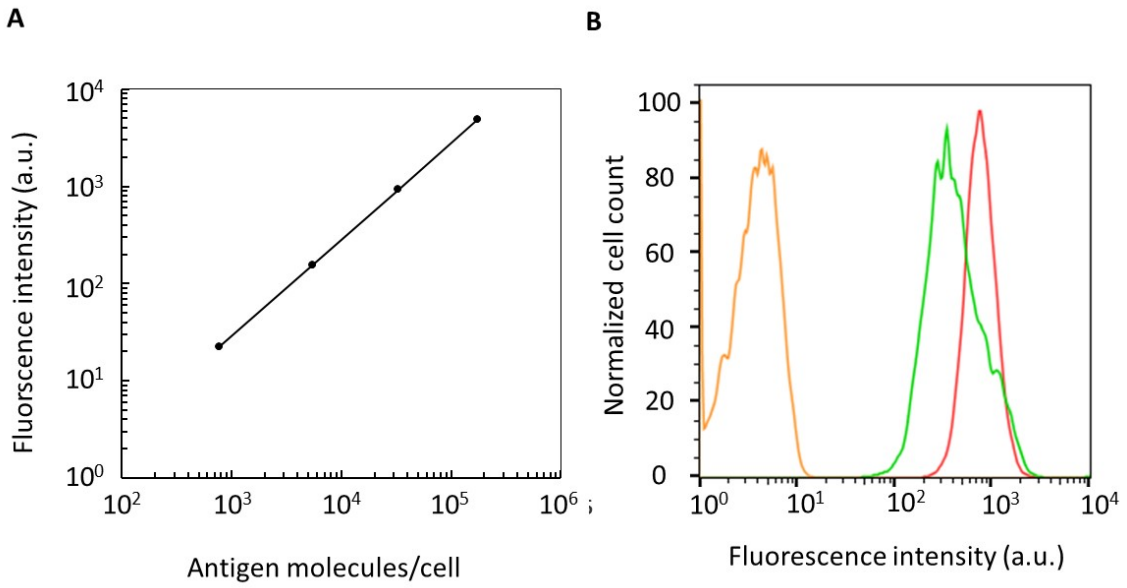

Figure S 13 : **(A)** Calibration curve with the secondary antibody and calibration beads (CellQuant calibrator kit, ref 7208, Biocytex). **(B)** Fluorescence histograms of T lymphocytes stained by indirect immunofluorescence with specific monoclonal antibodies CD49d (HP2/1) for VLA-4 (green) and CD11a (Hi111) for LFA-1 (red).

Model of swimming by membrane retrograde flow: ***Molecular paddling model***

The purpose of this section is to introduce a detailed model of the transfer of the cortex retrograde flow to the fluid surrounding the cell. The model is based on a mean-field approximation: we consider a region of a cell boundary that, on one hand, is large compared to the size of individual proteins, and, on the other hand, is sufficiently small compared to the cell scale. These assumptions allow us to consider the cell boundary to be flat and to represent all relevant quantities as a function of the distance from the cortex, averaging them over the two remaining coordinates. The freely diffuse and the cortex-bound proteins are thus modelled as a homogeneous porous medium with an effective viscous friction with the fluid. A similar model was considered[5] for a flow of fluid inside a brush of polymers covering a wall and subject to an external flow. We therefore only list here the main ingredients of the solution and final results.

The following analysis is written in the reference frame comoving with the phospholipid bilayer. We consider the actin-bound proteins to move with the cortex velocity v_a, as suggested by our measurements showing that high affinity integrins LFA-1 are advected at a speed very close to the one of actin cortex (Figure 7-I), and we call v_p the speed of proteins not bound to actin. The exact numbers of advected and non advected proteins are however not known precisely. Finally, we

assume that the individual protein molecules interact only via hydrodynamic fields in the outside fluid, thus excluding short-range solid friction between them. The proteins also interact via hydrodynamic fields inside the bilayer. However, since the net velocity of the bilayer is zero in the chosen frame, this interaction would only result in a correlation of velocities in pairs of proteins located closely to each other. This would represent a higher-order effect in the concentration of cortex-bound proteins than the one considered here.

The protein brush can be modelled by the Brinkman equations[6], which can easily be motivated as follows. The fluid in the brush is to leading order function only of the coordinate z orthogonal to the cell membrane (since the brush thickness is small as compared to the cell size), and obeys the one-dimensional nonhomogeneous Stokes equation

Equation 18 $$\eta_0 \partial_{zz} v_{fx}(z) + f_x(z) = 0,$$

Where $f(z)$ is the volume-related force density applied by the brush on the fluid, given by

Equation 19 $$f_x(z) = \xi_i\big[v_a - v_{fx}(z)\big] + \xi_p\big[v_p - v_{fx}(z)\big],$$

where $\xi_i = \varphi_i^{2D}\,\zeta_i/V_i$ is the volume-averaged drag coefficient of actin-bound proteins (e.g. integrins LFA-1 in the experimental part) and $\xi_p = \varphi_p^{2D}\,\zeta_p/V_p$ is the volume-averaged drag coefficient of passively advected proteins (e.g. MHC-1 in the experimental part). Here φ^{2D} is the area fraction of corresponding proteins, ζ is the corresponding viscous drag coefficient, and V is the volume of the extramembrane part of the corresponding protein.

The velocity of the free proteins, v_p, is calculated by requiring the sum of drag forces applied by them on the fluid and the bilayer to be equal to zero, which gives a condition:

Equation 20 $$f_x^{bl} h^{bl} + \xi_p \int \big[v_p - v_{fx}(z')\big]\, dz' = 0,$$

where h is the thickness of the brush and h_{bl} is the thickness of the bilayer. The drag experienced by the freely advected protiens from the phospholipids of the bilayer f_x^{bl} is expressed as

Equation 21 $$f_x^{bl} = \xi_{bl} v_p,$$

where $\xi_{bl} = \varphi_p^{2D}\,\zeta_{bl}/V_{bl}$ is the volume-averaged drag coefficient inside the bilayer for passively advected proteins, ζ_{bl} is the corresponding Stokes drag coefficient for one protein, and V_{bl} is the volume of the protein part inside the bilayer. Note that the cortex-bound proteins experience drag inside the bilayer just as the passive ones do but their velocity is fully determined by the flow of the cortex, to which they are firmly attached.

Equation 18 and Equation 19 can be solved for v_{fx} as a function of v_a and v_p by using the two boundary conditions:

Equation 22 $$v_{fx}(0) = 0, \quad \text{and} \quad \partial_z v_{fx}(h) = 0.$$

Equation 20 and Equation 21 yield the expression of v_p as a function of v_a, and thus the full expression of the fluid velocity field as a function of drag coefficients, the membrane thickness and v_a. From this knowledge we determine β (which is the transmission coefficient of the cortex flow to the fluid at the brush surface, $z = h$). β is function of the drag coefficients and the viscosities. The explicit forms of β, v_p, and v_{fx} read

Equation 23 $$\beta = \frac{\xi_a v_a + \xi_p v_p}{\xi_a + \xi_p}\left[1 - \frac{2g}{1+g^2}\right],$$

Equation 24 $$v_p = \xi_p \xi_i v_a \frac{\lambda h\left(1+g^2\right)+1-g^2}{\xi_p^2(g^2-1)+\left(\xi_i \xi_p h + h_{bl}\xi_{bl}\left(\xi_i+\xi_p\right)\right)\lambda(1+g^2)},$$

Equation 25 $$v_{fx} = \frac{\xi_i v_a + \xi_p v_p}{\xi_i + \xi_p}\left[1 - \frac{e^{\lambda z}+g^2 e^{-\lambda z}}{1+g^2}\right],$$

where $\lambda^2 = \left(\xi_i + \xi_p\right)/\eta_0$ and $g = e^{\lambda h}$.

The Stokes drag coefficients of the proteins in the outer fluid are written as $\zeta = 6\pi R_h \eta_0 \approx 10^{-10}\, kg/s$, where R_h is the Stokes radius, which we take here as 6 nm for simplicity. The Stokes drag coefficient in bilayer can be estimated directly from the measurements of the diffusion coefficient D_t^{2D} of MHC-1 freely advected proteins : $\zeta_{bl} = k_B\, T/D_t^{2D} \approx 10^{-8}\, kg/s$. The thickness of the bilayer is taken as 8 nm. The brush thickness is taken as 20 nm, which we estimate from the length of integrins in activated state. The volume of the external part of the proteins is taken as $V_i = V_p = 4\,\pi R_h^3/3 \approx 900 nm^3$. The volume of the bilayer segment of the passively advected proteins is estimated as $V_{bl} = \pi R_h^2 h_{bl} \approx 900 nm^3$. Supplemental Figure S 14 shows the transmission coefficient β and $\beta_p = v_p/v_a$ as a function of the concentration φ_p^{2D}.

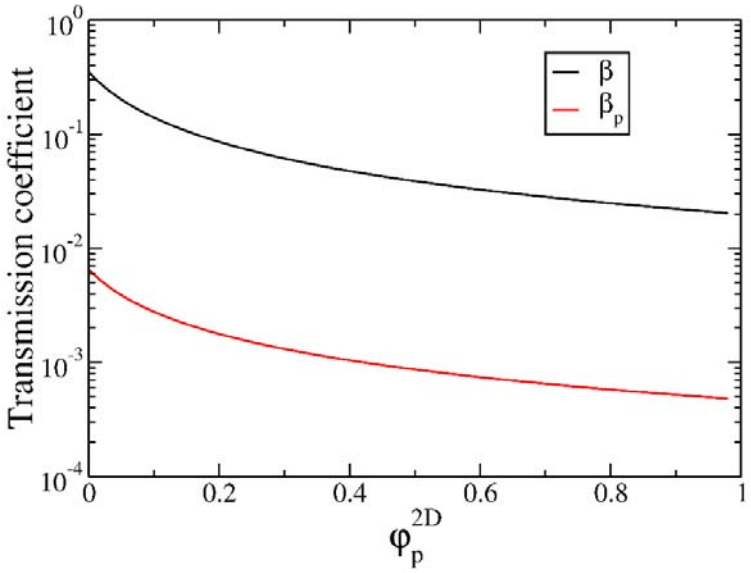

Figure S 14 : Transmission coefficients of the cortex flow to the fluid β (black curve) and to non advected proteins β_p (red curve) as a function of the concentration φ_p^{2D}, as given by Equation 23 and Equation 24. $R_h = 6nm, \eta_0 = 0.001Pa \cdot s,\ \ h = 20nm,\ \ \varphi_i^{2D} = 2\%, \zeta_{bl} = 10^{-8}\, kg/s$.

The analysis above was performed in the reference frame of the phospholipid bilayer. The experimental results do not allow us to establish whether a significant retrograde flow of the phospholipids is present in the reference frame of the cell membrane. Assuming the average local velocity of the phospholipids v_{bl} in the reference frame of the cell membrane is known, we can express the velocity fields in the reference frame of the swimmer membrane as $v_f + v_{bl}$ for fluid velocity, as$v_p + v_{bl}$ for freely diffusing proteins and as $v_a + v_{bl}$. The full expression for transmission coefficient is then written as $\beta(v_{bl}) = \beta(0) + \frac{v_{bl}}{v_a}\big(1 - \beta(0)\big)$, where $\beta(0)$ is given by Equation 26 and v_a is measured in the reference frame of the cell membrane. This shows that allowing for retrograde flow of the bilayer further increases the transmission coefficient.

BIBLIOGRAPHY

1. Saintillan, D. & Shelley, M. J. Active suspensions and their nonlinear models. *Comptes Rendus Phys.* **14**, 497–517 (2013).

2. Manurung, A. Elliptic fourier for shape analysis (https://www.mathworks.com/matlabcentral/fileexchange/32800-elliptic-fourier-for-shape-analysis). (2020).
3. Farutin, A., Biben, T. & Misbah, C. 3D numerical simulations of vesicle and inextensible capsule dynamics. *J. Comput. Phys.* **275**, 539–568 (2014).
4. Pozrikidis, C. Boundary Integral and Singularity Methods for Linearized Viscous Flow - doi:10.1017/CBO9780511624124. in (Cambridge University Press., 1992).
5. Kim, Y. W. *et al.* Nonlinear Response of Grafted Semiflexible Polymers in Shear Flow. *Macromolecules* **42**, 3650–3655 (2009).
6. Brinkman, H. C. A calculation of the viscous force exerted by a flowing fluid on a dense swarm of particles. *Flow Turbul. Combust.* **1**, 27 (1949).